Extricating human tumor-unique immune alterations from non-malignant tissue inflammation

Martin Prlic (mprlic@fredhutch.org)
Fred Hutchinson Cancer Research Center https://orcid.org/0000-0002-0685-9321
Florian Mair
Fred Hutchinson Cancer Research Center https://orcid.org/0000-0001-6732-5449
Jami Erickson
Fred Hutchinson Cancer Research Center https://orcid.org/0000-0002-4549-5217
Marie Frutoso
Fred Hutchinson Cancer Research Center
Evan Greene
Fred Hutchinson Cancer Research Center
Valentin Voillet
Hutchinson Centre Research Institute of South Africa
Andrew Konecny
Fred Hutchinson Cancer Research Center
Douglas Dixon
School of Dentistry, University of Washington
Brittany Barber
Head and Neck Surgery Center, University of Washington
Raphael Gottardo
Fred Hutchinson Cancer Research Center https://orcid.org/0000-0002-3867-0232

Biological Sciences - Article

Keywords: immunotherapies, cancer, inflammation

Posted Date: May 17th, 2021

DOI: https://doi.org/10.21203/rs.3.rs-356214/v1

Extricating human tumor-unique immune alterations from non-malignant tissue inflammation

Florian Mair[#1], Jami R. Erickson[#1], Marie Frutoso[1], Evan Greene[1], Valentin Voillet[1,4], Andrew Konecny[1], Douglas Dixon[2§], Brittany Barber[3], Raphael Gottardo[1,5] and Martin Prlic[1,6*]

[1] Fred Hutchinson Cancer Research Center, Vaccine and Infectious Disease Division, Seattle, WA 98109, USA.

[2] Department of Periodontics, School of Dentistry, University of Washington, Seattle, WA, 98195, USA.

[3] Head and Neck Surgery Center, University of Washington, Seattle, WA, 98195, USA.

[4] Cape Town HVTN Immunology Laboratory, Hutchinson Centre Research Institute of South Africa, NPC (HCRISA), Cape Town, South Africa.

[5] Department of Statistics, University of Washington, Seattle, WA 98195, USA.

[6] Department of Immunology and Department of Global Health, University of Washington, Seattle, WA 98195, USA.

[§] Present address: Department of Periodontics, University of Tennessee Health Science Center, College of Dentistry, Memphis TN, 38163.

[#]These authors contributed equally

* Correspondence: mprlic@fredhutch.org

Abstract:

Immunotherapies to treat cancer have achieved remarkable successes, but major challenges persist [1,2]. An inherent weakness of current treatment approaches is that therapeutically targeted pathways are not only found in tumors, but also in tissue microenvironments, particularly inflamed tissues. This confounding overlap complicates treatment as well as predictions of treatment outcome [3,4]. In an effort to identify potential tumor-unique immunotherapeutic targets that are distinct from general tissue inflammation, we used complementary single-cell analysis approaches to interrogate immune cell alterations and interactions in human squamous cell carcinomas and site-matched non-malignant, inflamed tissues. We found that a distinct population of intratumoral regulatory T cells (Tregs) received T cell receptor (TCR) signals from antigen-presenting cells and this Treg population was uniquely identified by co-expression of ICOS and IL-1 receptor type 1 (IL-1R1). Intratumoral IL-1R^{+} Tregs appeared activated and a TCR signal was sufficient to convert IL-1R1^{-} Tregs to IL-1R1^{+} Tregs *ex vivo*. Overall, our work identifies an intratumoral Treg population that recognizes antigen in the tumor microenvironment and two biomarkers that allow for specific depletion of these Tregs. Finally, our approach also provides a blueprint for extricating tumor-unique therapeutic targets distinct from general inflammatory patterns in other tumors.

Main Text:

Antigen-presenting cells (APCs) and T cells residing in non-lymphoid tissues adapt distinct phenotypic and functional properties relative to their circulating counterparts in the peripheral blood [5,6]. These immune cells respond to tissue damage or invading pathogens with a tightly regulated effector program [6,7] and are also present in many solid tumors types, where they are thought to be critical determinants of tumor development and disease outcome [1,8]. One hallmark of immune-infiltrated human tumor tissues is the presence of an inflammatory microenvironment, which has been extensively scrutinized during the past decade [3,9]. However, despite these efforts it remains unclear which immune cell subsets and signaling pathways in the human tumor microenvironment are distinct from general inflammatory processes that occur in other tissues.

One of the best studied immune populations in tumor tissues are functionally exhausted (dysfunctional) T cells and regulatory T cells (Tregs), both of which are considered pivotal factors for inefficient anti-tumor immune responses [10,11]. These T cell subsets express immuno-inhibitory molecules such as programmed death 1 (PD-1) or cytotoxic T-lymphocyte-associated antigen 4 (CTLA-4), which are the focus of various immunotherapeutic approaches [12]. However, expression of PD-1 and CTLA-4 is not limited to tumor-infiltrating T cells, but also found on T cells in non-malignant tissues during homeostasis and inflammation [6,13]. Importantly, the effector program of T cells and their expression of immuno-regulatory molecules is closely linked to the function of antigen-presenting cells (APCs) , including dendritic cells (DCs), macrophages and other monocyte-derived cells [14]. APCs integrate tissue-specific and inflammation-

dependent cues from the microenvironment, either enhancing or suppressing local T cell responses [15]. Thus, functional alteration of APCs in the human tumor microenvironment has been suggested as an additional promising therapeutic target [16,17].

We hypothesized that comparing the human tumor microenvironment to non-malignant, inflamed tissues could reveal truly tumor-unique immune alterations that could help reveal why some tumors do not respond to immune checkpoint inhibitors and could even lead to the identification of novel therapeutic targets. Head and neck squamous cell carcinomas (HNSCC) have a large immune infiltrate, but most patients do not respond to treatment with immune checkpoint inhibitors [18]. We thus combined several single-cell analysis pipelines to generate a comprehensive immune landscape of human HNSCC with site matched non-malignant inflamed tissues. Our data revealed substantial congruence of the immune phenotypes between these tissue groups, but computational analysis approaches identified tumor-unique subsets of activated APCs and Tregs. Predicted interaction patterns of APCs and Tregs included MHC–TCR and IL-1–IL-1R signaling. *Ex vivo* experiments confirmed these computational predictions. IL-1R1$^+$ Tregs showed hallmarks of increased immunosuppressive function and recent TCR stimulation. Finally, these tumor-unique Tregs could be identified among all hematopoietic cells by the combined expression of IL-1R1 and ICOS, thus allowing for specific intratumoral depletion of these Tregs by bispecific antibodies or logic-gated CAR T cells, which could ultimately help restore anti-tumor immune responses.

The immune phenotypes in inflamed non-malignant OM tissues largely resemble those of HNSCC tumors

Surgery is typically the first line of treatment for head and neck squamous cell carcinoma (HNSCC), which is the umbrella term encompassing oral and oropharyngeal squamous cell carcinoma [19]. Non-malignant inflamed oral mucosal (OM) tissues (typically without prior anti-inflammatory treatment) from oral surgeries served as our reference. Together, this allowed us to compare the immune infiltrate of human inflamed vs. tumor tissues without prior therapeutic interventions as a confounding variable (detailed sample information listed in Suppl. Table 1).

First, we fully catalogued the immune landscape in OM and HNSCC tissues by using two 30-parameter flow cytometry panels (Fig. 1a and Suppl. Table 2) (adapted from [20]). The frequency of $CD3^+$ T cells, $CD19^+$ B cells and $CD56^+$ NK cells among total $CD45^+$ live cells as well as the CD4/CD8 ratio was essentially equivalent between OM and HNSCC tissues (Ext. data Fig. 1a). Recent findings suggest that cytotoxic $CD8^+$ T cells with a tissue-resident memory phenotype can be a principal predictor for tumor progression [8,21,22]. The expression patterns of the tissue residency markers CD69 and CD103 were very similar between OM and HNSCC tissues (Fig. 1b). PD-1, a biomarker of exhausted T cells [23] was expressed by approximately 50% of total $CD8^+$ T cells both in OM and HNSCC tissue samples (Fig. 1c). The transcription factor TCF-1, CD39 and the majority of all other markers for $CD4^+$ and $CD8^+$ T cells showed similar expression (Fig. 1d and Ext. data Fig. 1b and 1c) in OM as well as HNSCC infiltrating T cells.

Next, we quantified subsets of monocytes and dendritic cells in the tumor microenvironment based on canonical lineage markers: $CD14^+$ monocyte/macrophage-

like cells, CD11c$^+$ CD141$^+$ cross-presenting cDC1s, CD11c$^+$ CD1c$^+$ CD163$^-$ cDC2s, CD11c$^+$ CD1c$^+$ CD163$^+$ DC3s (previously referred to as inflammatory DCs [24,25,26]) and CD16$^+$ non-conventional monocytes (Fig. 1e and Ext. data Fig. 2a)). While the relative abundance of CD14$^+$ cells as well as total CD14$^-$CD3$^-$CD19$^-$ (hereafter referred to as lin$^-$) HLADR$^+$ cells was indistinguishable between OM and HNSCC tissues, we noted a slight decrease in the frequency of CD141$^+$ cDC1s in HNSCC [27]. Contrary, cDC2s, DC3s and CD16$^+$ cells were present in OM and HNSCC tissues with similar frequencies (Fig. 1e). Overall, we observed substantial phenotypic heterogeneity across subsets (Ext. data Fig. 2b) but similar expression patterns for the CD206 (Fig. 1f) on CD14$^+$ cells across the different tissues, indicating that M2-like phenotypes are not a specific hallmark of the tumor microenvironment [28]. A comparison of all biomarkers in our panel showed that tissue-infiltrating cells had a markedly different phenotype relative to their circulating blood counterparts, but were relatively similar between OM and HNSCC tissues (Fig. 1g and Ext. data Fig 2c).

Taken together, these data indicate substantial phenotypic congruence of the T cell and APC immune infiltrate in inflamed OM and HNSCC. Next, we wanted to determine if single-cell RNA-sequencing (scRNA-seq) could identify transcriptionally tumor-unique T cell and APC populations.

Comprehensive single-cell RNAseq analysis of OM and HNSCC immune infiltrates reveals subset-specific cytokine modules in the APC compartment

To ensure that our analysis would encompass also rare T cell and APC subsets, we sorted pan CD3$^+$ T cells as well as lin$^-$ HLA-DR$^+$ cells from OM and HNSCC tissues with

matched blood from multiple donors (gating strategy in Ext. data Fig. 3a and 3b). After QC and data integration using Harmony [29] we obtained a total of approximately 140.000 cells (from 8 donors), providing one of the most comprehensive data sets covering human tissue-derived T cells and APCs to date. After dimensionality reduction using UMAP [30] and cellular annotation using SingleR [31], canonical T cell and APC populations clearly separated by UMAP (Fig. 2a). OM and HNSCC-derived cells grouped together, but separate from peripheral blood (Fig. 2b) in line with the phenotypic overlap found in our flow cytometry data.

Subsetting and re-clustering APCs revealed eight distinct populations, which were mapped to established lineages (Fig. 2c) including cDC2s and DC3s. Of note, we also identified a population of cells expressing high levels of CCR7, CCL19 and the GM-CSF receptor (CSF2A), resembling recently described “mature DCs enriched in immunoregulatory molecules” (mregDCs) [32]. Importantly, mregDCs were present both in OM and HNSCC with comparable abundance indicating that this DC subset is present in inflamed tissues and not exclusive to tumors. Furthermore, we found a population of HLA-DR expressing mast cells in HNSCC tissues, expressing the signature genes CLU (mast cell carboxypeptidase A) and GATA2 (Fig. 2c, d).

We observed relatively consistent distribution of these clusters across the different donors and tissue sources (Fig. 2d). Peripheral blood samples were primarily comprised of monocytes with a classical (i.e. $CD14^{+}$) and non-classical (i.e. $FCGR3A^{+}$) phenotype, as well as cDC2s and pDCs (Fig. 2e). In contrast, all OM and HNSCC tissues harbored a major proportion of DC3s, cDC1s as well as mregDCs (Fig. 2e).

To characterize the functional profile of these tissue APCs, we plotted the normalized transcript abundance of key co-regulatory genes and cytokines for the OM- and HNSCC-derived cells (Fig. 2f). We noted that modules of lymphocyte-attracting chemokine transcripts (CXCL2/3 as well as CXCL16 and CCL3) were mostly shared among the monocyte, cDC2 and DC3 clusters, with monocyte/macrophage like cells expressing the highest levels. The chemokine transcripts CCL17 and CCL22 as well as EBI-3 were primarily detected in mregDCs.

Next, we wanted to assess how the transcriptional properties of these APC clusters changed in HNSCC relative to the inflamed OM. Identification of DE genes using model-based analysis of single-cell transcriptomics (MAST) [33] revealed that only DC3s and cDC1s showed a pronounced adaptation of their transcriptome in HNSCC (i.e. more than 150 genes) (Fig. 2g). DC3s expressed CD14 across all tissue sources and showed a general tissue-specific inflammatory profile both in OM and HNSCC, with high expression of CCL4 and IL1B (Fig. 2h, left panel). Among the transcripts most enriched in HNSCC DC3s were the chemokine CXCL16 and TGFB1. For cDC1s, some of the general tissue-specific inflammatory genes were CXCL8 (IL-8) and TNF, while the tumor-enriched transcripts included IL18BP (recently proposed as a checkpoint molecule [34]) and Osteopontin (Fig. 2h, right panel).

NicheNet analysis predicts tumor-unique T cell specific crosstalk between tumor-infiltrating APCs and T cells

Our approaches so far highlight congruencies and some differences between tumors and inflamed tissues. To further pinpoint tumor-unique immune alterations, we wanted

156 to identify potential tumor-unique cross-talk between T cells and APCs using NicheNet
157 [35]. For this, we leveraged the ability of NicheNet to predict ligand-receptor interactions
158 based only on differentially expressed genes in the HNSCC vs. OM-derived T cells
159 (workflow outlined in Fig. 3a). We set our scRNA-seq derived APC clusters (excluding
160 pDCs and mast cells) as the sender population, and the $CD4^+$ T cell, $CD8^+$ T cell, and
161 $CD4^+$ Treg clusters as separate receiver populations. For each T cell subset, we
162 focused our analysis on the top 20 ligand-receptor pairs identified by NicheNet and
163 visualized these interactions as circos plots (Fig. 3b). We arbitrarily sub-divided these
164 interactions into 3 groups (unique/interesting, cytokine/co-receptor and other) for the
165 sole purpose of helping with visualization. We further highlighted some ligand-receptor
166 pairs of interest (bold, underlined) across all T cell subsets. Remarkably, NicheNet
167 predicted that four ligand-receptor interactions were unique between the APC and
168 Treg population in HNSCC: ICOS ligand (ICOSLG) via ICOS, the cytokines IL-15
169 through the IL2RG and IL2RB receptor complex, the pro-inflammatory cytokines IL-18
170 via the IL18-R1 and IL-1B via the IL-1 receptors type 1 and type 2 (Fig. 3b, right panel).
171 Furthermore, Nichenet also predicted TCR signaling in the Treg compartment, via the
172 TCRzeta-chain (CD247) and CD3G (Figure 3b, right panel).
173 We were most intrigued by the predicted TCR and IL-1 signaling events given that the
174 Treg population in human HNSCC is expanded and expansion of the Treg
175 compartment has been associated with transient immune checkpoint inhibitor
176 treatment effects in an HNSCC mouse model [36]. Thus, we further interrogated the
177 accuracy and relevance of these interactions in a series of *ex vivo* experiments. We first
178 asked if IL-1 could be present in the tumor. After *ex-vivo* culture in the presence of

Brefeldin A only, a majority of $CD14^+$ monocyte/macrophage like cells expressed IL-1β as well as IL-1α protein, as did up to 20% of the pan cDCs (Fig. 3c). As expected, $CD123^+$ pDCs did not express IL-1α/β. To address whether IL-1 is available in the tumor microenvironment, we performed Luminex analysis of flash-frozen whole tumor lysate, which revealed significant levels of IL-1α, IL-1β and IL-18 (Fig. 3d). Together, these data indicate that an intratumoral IL-1 signal is feasible. Next, we tested if the predicted "receiver" receptors are expressed by T cells using an additional 30 parameter flow cytometry panel (Suppl. Table 2). We found that IL-1R1 was specifically expressed by tumor-infiltrating Tregs, but neither by tumor infiltrating $CD4^+$ T cells or $CD8^+$ T cells, nor by T cells in the peripheral blood (Fig. 3e). Importantly, up to 60% of the Tregs expressed IL-1R1, while expression of IL-1R2, which is thought to be a decoy receptor for IL-1 signaling, was detectable on less than 3% of cells. We further analyzed the phenotype of IL-$1R1^+$ Tregs and found that nearly all IL-$1R1^+$ Tregs were co-expressing ICOS and HLA-DR, and higher levels of the chemokine receptor CXCR6 (Fig. 3f). We next asked if the combined expression of IL-1R1 and ICOS could uniquely identify Tregs among all hematopoietic ($CD45^+$) cells in HNSCC and blood. We found that nearly all of cells in the $CD45^+$ IL-$1R1^+$ $ICOS^+$ gate were $CD3^+$ $CD4^+$ $CD25^+$ $CD127^-$ Tregs (Fig. 3g). These data suggest that a large fraction of Tregs in the tumor could be directly targeted and depleted by only using these two cell surface-expressed proteins. Thus, we next wanted to determine if these Tregs are a potentially clinically relevant target and further explore a possible link between IL-1R1 expression and the predicted TCR signaling events.

IL-1R1-expressing Tregs represent a functionally distinct Treg population with hallmarks of recent TCR stimulation

To further define IL-1R1^{+} and IL-1R1^{-} Tregs and assess the biological relevance of IL-1R1^{+} Tregs, we used a targeted transcriptomics approach [37] to measure expression of 495 pre-selected genes (Suppl. Table 3) on sorted IL-1R1^{+} and IL-1R1^{-} Tregs from three HNSCC tumor donors, identifying two transcriptionally distinct populations of regulatory T cells in the tumor that were separate from peripheral blood Tregs (Fig 4a). The cluster corresponding to IL-1R1^{+} Tregs (orange) was also marked by high expression of TNFRSF18 (Glucocorticoid-induced TNF receptor, GITR) and TNFRSF9 (4-1BB), which has been suggested as a pan-cancer Treg target [38]. Furthermore, the IL-1R1^{+} cluster showed exclusive expression of the chemokine receptors CXCR6 and CCR8 as well as CD39 and the transcription factor ID3, which has been implicating in formation of a tissue-resident Treg program [39] (Fig. 4b).

To further determine whether IL-1R1^{+} Tregs are indeed functional, we performed an *ex vivo* stimulation experiment using AbSeq as a read-out for changes in transcript and surface protein expression. After data integration with Harmony [29] we identified two main CD4^{+} T cell clusters and two Treg clusters based on surface protein and transcript profile (Fig. 4c). Of note, an additional cluster of proliferating cells (high in TOP2A and MKI67) aligned with the IL-1R1^{+} Treg cluster thus indicating a potential close relationship (Fig. 4c). CD25^{+}CD127^{-} Tregs responded to PMA-Ionomycin stimulation by robust upregulation of CTLA4 and CD40L transcript indicating that Tregs are functional and respond as expected (Fig. 4d). Importantly, these CTLA4-high Tregs were mostly found in the IL1R1^{+}ICOS^{+} population (Fig. 4e).

Based on the NicheNet predictions (Fig. 3b) we considered that IL-1R1^{+} Tregs in the tumor could represent a population receiving TCR signals. To determine a possible link between TCR signaling and IL-1R1 expression, we sort-purified Tregs from peripheral blood of healthy donors, and IL-1R1^{-} and IL-1R1^{+} Tregs isolated from HNSCC. These sorted Treg populations were then stimulated with anti-CD3/CD28 beads. We observed robust upregulation of IL-1R1 surface expression on all IL-1R1^{-} Tregs, including IL-1R1^{-} Tregs isolated from HNSCC tissues (Fig. 4f). These data indicate that a TCR signal is sufficient to elicit IL-1R1 expression by human Tregs and also suggest that IL-1R1 expression on Tregs can be an indicator for recent or active TCR signaling. In contrast, IL-1R2 expression was more limited (Fig. 4f) suggesting that the decoy receptor is unlikely to interfere with IL-1 signals.

Discussion

Overall, our data revealed that many immune phenotypes typically associated with the human tumor microenvironment were also found in non-malignant, inflamed tissues. The expression pattern of PD-1, a key checkpoint inhibitory molecule that is the target of many therapeutic strategies was essentially identical on T cells in tumor tissues and non-malignant, inflamed tissues, which could offer an explanation for the at times severe side-effects of systemic anti-PD-1 treatment [2,40]. Of note, PD-1 expression is typically considered to be driven by T cell receptor signals, but also upregulated by pro-inflammatory cytokines [41], which may explain the high expression levels in inflamed tissues. Similarly, our data indicated that recently described mregDCs [32] are not tumor-unique, given their presence in non-malignant, inflamed tissues, with minimal

transcriptional changes between these tissues. Overall, this highlights that studying inflamed human tissues can provide a critical reference point for extricating tumor-unique changes from general inflammatory immune adaptation.

While assessing the immune landscapes of HNSCC and OM tissues revealed many congruencies, it also provided first hints that tumor-unique immune adaptations may exist. cDC1s and particularly DC3s were the two main APC subsets showing tumor-specific adaptation of their chemokine and cytokine expression profile. NicheNet analysis of receptor-ligand interactions [35] predicted that Tregs in the tumor might actively receive TCR signals and specifically respond to a set of three cytokines: IL-1, IL-15 and IL-18. IL-18 has been implicated in inducing a tissue-repair program by secretion of Amphiregulin from IL18-R^{+} Tregs [42], and IL-15 has been shown to positively regulate expression of Foxp3 [43]. Much less is known about the effects of IL-1, traditionally considered a pro-inflammatory cytokine, on Tregs [44-46]. Our validation experiments revealed that a transcriptionally distinct subset of Tregs in the tumor expressed IL-1R1 protein. IL-1R1^{+} Tregs (compared to IL-1R1^{-} Tregs or CD4^{+} T cells) also expressed higher levels of the IL-18R1 and the chemokine receptor CXCR6 (Fig. 3f) suggesting that the predicted IL-18/IL18R1 and CXCL16/CXCR6 signaling axes in Tregs occur as well. Of note, CXCL16 was among the chemokine transcripts enriched in HNSCC-infiltrating DC3s (Fig. 2h). CXCR6 has previously been suggested to regulate migration of T_{RM} cells [47]. While ex vivo chemotaxis experiments were not feasible, it is still tempting to speculate that these chemokine-receptor pairs could also regulate Treg migration into the tumor microenvironment based on the increased transcript expression of the corresponding ligand CXCL16 in DC3s.

Our *ex vivo* restimulation experiments indicate that a TCR signal is sufficient to convert intratumoral IL-1R1^{-} Tregs into IL-1R1^{+} Tregs, and that IL-1R1^{+} Tregs represent a Treg population receiving TCR stimulation inside the tumor microenvironment. We observed an actively proliferating Treg cluster in the tumor microenvironment which phenotypically aligned with IL-1R1^{+} Tregs. This could suggest that some of these IL-1R1^{+} Tregs proliferate *in situ* after receiving a TCR signal from APCs. IL-1 has been shown to enhance CD4 T cell proliferation in a mouse model system [48], but if IL-1 plays a role in expanding Tregs in the tumor *in situ* is still unclear.

Our findings also have important implications for the design of future therapeutic strategies, since the specific depletion or functional modification of tumor-infiltrating Tregs is considered a promising anti-tumor therapy to reverse the immunosuppressive environment [49,50,51]. We show that the co-expression of IL-1R1 and ICOS is unique to this population of tumor-infiltrating Tregs and co-expression is not found on any other hematopoietically-derived (CD45^{+}) cells in the tumor or peripheral blood. Thus, our data also highlight a possible pathway for tumor-specific depletion of a large intratumoral Treg population using bi-specific antibodies or logic-gated chimeric antigen receptor (CAR) T cells [52]. Our data suggest that this depletion would be rather tumor-specific, given that the IL-1 and TCR signaling axis was highly enriched in HNSCC versus inflamed oral mucosa and given the lack of IL-1R1^{+} Tregs in the periphery.

Finally, our general experimental and analysis approach can also serve as a blueprint to define tumor-unique adaptations in other solid tumors, laying the basis for more specific anti-tumor therapies and an improved understanding of tumor-unique inflammatory processes.

References:

1 Chen, D. S. & Mellman, I. Oncology meets immunology: the cancer-immunity cycle. *Immunity* **39**, 1-10, doi:10.1016/j.immuni.2013.07.012 (2013).

2 Martins, F. *et al.* Adverse effects of immune-checkpoint inhibitors: epidemiology, management and surveillance. *Nature reviews. Clinical oncology* **16**, 563-580, doi:10.1038/s41571-019-0218-0 (2019).

3 Greten, F. R. & Grivennikov, S. I. Inflammation and Cancer: Triggers, Mechanisms, and Consequences. *Immunity* **51**, 27-41, doi:10.1016/j.immuni.2019.06.025 (2019).

4 Mujal, A. M. & Krummel, M. F. Immunity as a continuum of archetypes. *Science* **364**, 28-29, doi:10.1126/science.aau8694 (2019).

5 Fan, X. & Rudensky, A. Y. Hallmarks of Tissue-Resident Lymphocytes. *Cell* **164**, 1198-1211, doi:10.1016/j.cell.2016.02.048 (2016).

6 Kumar, B. V. *et al.* Human Tissue-Resident Memory T Cells Are Defined by Core Transcriptional and Functional Signatures in Lymphoid and Mucosal Sites. *Cell reports* **20**, 2921-2934, doi:10.1016/j.celrep.2017.08.078 (2017).

7 Szabo, P. A. *et al.* Single-cell transcriptomics of human T cells reveals tissue and activation signatures in health and disease. *Nature communications* **10**, 4706-4716, doi:10.1038/s41467-019-12464-3 (2019).

8 Amsen, D., van Gisbergen, K. P. J. M., Hombrink, P. & van Lier, R. A. W. Tissue-resident memory T cells at the center of immunity to solid tumors. *Nature Immunology* **19**, 538-546, doi:10.1038/s41590-018-0114-2 (2018).

9 Ji, A. L. *et al.* Multimodal Analysis of Composition and Spatial Architecture in Human Squamous Cell Carcinoma. *Cell* **182**, 497-514.e422, doi:10.1016/j.cell.2020.05.039 (2020).

10 Scott, A. C. *et al.* TOX is a critical regulator of tumour-specific T cell differentiation. *Nature* **571**, 270-274, doi:10.1038/s41586-019-1324-y (2019).

11 Chao, J. L. & Savage, P. A. Unlocking the Complexities of Tumor-Associated Regulatory T Cells. *J Immunol* **200**, 415-421, doi:10.4049/jimmunol.1701188 (2018).

12 Sharma, P. & Allison, J. P. Dissecting the mechanisms of immune checkpoint therapy. *Nat Rev Immunol* **20**, 75-76, doi:10.1038/s41577-020-0275-8 (2020).

13 Woodward Davis, A. S. *et al.* The human tissue-resident CCR5+ T cell compartment maintains protective and functional properties during inflammation. *Science translational medicine* **11**, eaaw8718, doi:10.1126/scitranslmed.aaw8718 (2019).

14 Guilliams, M. *et al.* Dendritic cells, monocytes and macrophages: a unified nomenclature based on ontogeny. *Nature Reviews Immunology* **14**, 571-578, doi:10.1038/nri3712 (2014).

15 Baßler, K., Schulte-Schrepping, J., Warnat-Herresthal, S., Aschenbrenner, A. C. & Schultze, J. L. The Myeloid Cell Compartment-Cell by Cell. *Annual Review of Immunology* **37**, 269-293, doi:10.1146/annurev-immunol-042718-041728 (2019).

16 Binnewies, M. *et al.* Unleashing Type-2 Dendritic Cells to Drive Protective Antitumor CD4+ T Cell Immunity. *Cell* **177**, 556-571.e516, doi:10.1016/j.cell.2019.02.005 (2019).

17 Wculek, S. K. *et al.* Dendritic cells in cancer immunology and immunotherapy. *Nature Reviews Immunology* **144**, 646-618, doi:10.1038/s41577-019-0210-z (2019).

18 Qian, J. M. & Schoenfeld, J. D. Radiotherapy and Immunotherapy for Head and Neck Cancer: Current Evidence and Challenges. *Front Oncol* **10**, 608772, doi:10.3389/fonc.2020.608772 (2020).

19 Chow, L. Q. M. Head and Neck Cancer. *The New England journal of medicine* **382**, 60-72, doi:10.1056/NEJMra1715715 (2020).

20 Mair, F. & Prlic, M. OMIP-044: 28-color immunophenotyping of the human dendritic cell compartment. *Cytometry A* **106**, 255, doi:10.1002/cyto.a.23331 (2018).

21 Duhen, T. *et al.* Co-expression of CD39 and CD103 identifies tumor-reactive CD8 T cells in human solid tumors. *Nature communications* **9**, 2724, doi:10.1038/s41467-018-05072-0 (2018).

22 (kConFab), K. C. F. C. f. R. i. F. B. C. *et al.* Single-cell profiling of breast cancer T cells reveals a tissue-resident memory subset associated with improved prognosis. *Nature medicine* **24**, 986-993, doi:10.1038/s41591-018-0078-7 (2018).

23 Blank, C. U. *et al.* Defining 'T cell exhaustion'. *Nature Reviews Immunology* **19**, 665-674, doi:10.1038/s41577-019-0221-9 (2019).

24 Bourdely, P. *et al.* Transcriptional and Functional Analysis of CD1c+ Human Dendritic Cells Identifies a CD163+ Subset Priming CD8+CD103+ T Cells. *Immunity* **53**, 335-352.e338, doi:10.1016/j.immuni.2020.06.002 (2020).

25 Segura, E. & Amigorena, S. Inflammatory dendritic cells in mice and humans. *Trends in Immunology* **34**, 440-445, doi:10.1016/j.it.2013.06.001 (2013).

26 Dutertre, C.-A. *et al.* Single-Cell Analysis of Human Mononuclear Phagocytes Reveals Subset-Defining Markers and Identifies Circulating Inflammatory Dendritic Cells. *Immunity* **51**, 573-589.e578, doi:10.1016/j.immuni.2019.08.008 (2019).

27 Salmon, H. *et al.* Expansion and Activation of CD103(+) Dendritic Cell Progenitors at the Tumor Site Enhances Tumor Responses to Therapeutic PD-L1 and BRAF Inhibition. *Immunity* **44**, 924-938, doi:10.1016/j.immuni.2016.03.012 (2016).

28 Lavin, Y. *et al.* Innate Immune Landscape in Early Lung Adenocarcinoma by Paired Single-Cell Analyses. *Cell* **169**, 750-765.e717, doi:10.1016/j.cell.2017.04.014 (2017).

29 Korsunsky, I. *et al.* Fast, sensitive and accurate integration of single-cell data with Harmony. *Nature Methods* **16**, 1289-1296, doi:10.1038/s41592-019-0619-0 (2019).

30 McInnes, L., Healy, J. & Melville, J. UMAP: Uniform Manifold Approximation and Projection for Dimension Reduction. (2018).

31 Aran, D. *et al.* Reference-based analysis of lung single-cell sequencing reveals a transitional profibrotic macrophage. *Nature Immunology* **20**, 163-172, doi:10.1038/s41590-018-0276-y (2019).

32 Maier, B. *et al.* A conserved dendritic-cell regulatory program limits antitumour immunity. *Nature* **580**, 257-262, doi:10.1038/s41586-020-2134-y (2020).

33 Finak, G. *et al.* MAST: a flexible statistical framework for assessing transcriptional changes and characterizing heterogeneity in single-cell RNA sequencing data. *Genome biology* **16**, 278, doi:10.1186/s13059-015-0844-5 (2015).

34 Zhou, T. *et al.* IL-18BP is a secreted immune checkpoint and barrier to IL-18 immunotherapy. *Nature* **583**, 609-614, doi:10.1038/s41586-020-2422-6 (2020).

35 Browaeys, R., Saelens, W. & Saeys, Y. NicheNet: modeling intercellular communication by linking ligands to target genes. *Nature Methods* **354**, 64-64, doi:10.1038/s41592-019-0667-5 (2019).

36 Oweida, A. *et al.* Resistance to Radiotherapy and PD-L1 Blockade Is Mediated by TIM-3 Upregulation and Regulatory T-Cell Infiltration. *Clin Cancer Res* **24**, 5368-5380, doi:10.1158/1078-0432.CCR-18-1038 (2018).

37 Mair, F. *et al.* A Targeted Multi-omic Analysis Approach Measures Protein Expression and Low-Abundance Transcripts on the Single-Cell Level. *Cell reports* **31**, 107499, doi:10.1016/j.celrep.2020.03.063 (2020).

38 Freeman, Z. T. *et al.* A conserved intratumoral regulatory T cell signature identifies 4-1BB as a pan-cancer target. *Journal of Clinical Investigation* **130**, 1405-1416, doi:10.1172/JCI128672 (2020).

39 Sullivan, J. M., Höllbacher, B. & Campbell, D. J. Cutting Edge: Dynamic Expression of Id3 Defines the Stepwise Differentiation of Tissue-Resident Regulatory T Cells.

Journal of immunology (Baltimore, Md. : 1950) **202**, 31-36, doi:10.4049/jimmunol.1800917 (2018).

40 Luoma, A. M. *et al.* Molecular Pathways of Colon Inflammation Induced by Cancer Immunotherapy. *Cell* **182**, 655-671 e622, doi:10.1016/j.cell.2020.06.001 (2020).

41 Kinter, A. L. *et al.* The common gamma-chain cytokines IL-2, IL-7, IL-15, and IL-21 induce the expression of programmed death-1 and its ligands. *The Journal of Immunology* **181**, 6738-6746, doi:10.4049/jimmunol.181.10.6738 (2008).

42 Arpaia, N. *et al.* A Distinct Function of Regulatory T Cells in Tissue Protection. *Cell* **162**, 1078-1089, doi:10.1016/j.cell.2015.08.021 (2015).

43 Tosiek, M. J., Fiette, L., El Daker, S., Eberl, G. & Freitas, A. A. IL-15-dependent balance between Foxp3 and RORγt expression impacts inflammatory bowel disease. *Nature communications* **7**, 1-11, doi:10.1038/ncomms10888 (2016).

44 Alvarez, F. *et al.* The alarmins IL-1 and IL-33 differentially regulate the functional specialisation of Foxp3+ regulatory T cells during mucosal inflammation. *Mucosal immunology* **12**, 746-760, doi:10.1038/s41385-019-0153-5 (2019).

45 Mercer, F., Kozhaya, L. & Unutmaz, D. Expression and Function of TNF and IL-1 Receptors on Human Regulatory T Cells. *PloS one* **5**, e8639, doi:10.1371/journal.pone.0008639 (2010).

46 Nikolouli, E. *et al.* Recirculating IL-1R2+ Tregs fine-tune intrathymic Treg development under inflammatory conditions. *Cellular & molecular immunology* **30**, 531, doi:10.1038/s41423-019-0352-8 (2020).

47 Wein, A. N. *et al.* CXCR6 regulates localization of tissue-resident memory CD8 T cells to the airways. *The Journal of experimental medicine* **216**, 2748-2762, doi:10.1084/jem.20181308 (2019).

48 Ben-Sasson, S. Z. *et al.* IL-1 acts directly on CD4 T cells to enhance their antigen-driven expansion and differentiation. *Proc Natl Acad Sci U S A* **106**, 7119-7124, doi:10.1073/pnas.0902745106 (2009).

49 Togashi, Y., Shitara, K. & Nishikawa, H. Regulatory T cells in cancer immunosuppression - implications for anticancer therapy. *Nature reviews. Clinical oncology* **16**, 356-371, doi:10.1038/s41571-019-0175-7 (2019).

50 Plitas, G., Rudensky, A. & 2020. Regulatory T Cells in Cancer. *annualreviews.org* **4**, 721-725, doi:10.1158/2326-6066.CIR-16-0193 (2016).

51 Simpson, T. R. *et al.* Fc-dependent depletion of tumor-infiltrating regulatory T cells co-defines the efficacy of anti–CTLA-4 therapy against melanoma. *Journal of Experimental Medicine* **210**, 1695-1710, doi:10.1084/jem.20130579 (2013).

52 Ebert, L. M., Yu, W., Gargett, T. & Brown, M. P. Logic-gated approaches to extend the utility of chimeric antigen receptor T-cell technology. *Biochem Soc Trans* **46**, 391-401, doi:10.1042/BST20170178 (2018).

53 Cossarizza, A. *et al.* Guidelines for the use of flow cytometry and cell sorting in immunological studies (second edition). *European journal of immunology* **49**, 1457-1973, doi:10.1002/eji.201970107 (2019).

54 Mair, F. & Tyznik, A. J. High-Dimensional Immunophenotyping with Fluorescence-Based Cytometry: A Practical Guidebook. *Methods in molecular biology (Clifton, N.J.)* **2032**, 1-29, doi:10.1007/978-1-4939-9650-6_1 (2019).

55 Perfetto, S. P., Ambrozak, D., Nguyen, R., Chattopadhyay, P. K. & Roederer, M. Quality assurance for polychromatic flow cytometry using a suite of calibration beads. *Nature protocols* **7**, 2067-2079, doi:10.1038/nprot.2012.126 (2012).

56 Erickson, J. R. *et al.* AbSeq Protocol Using the Nano-Well Cartridge-Based Rhapsody Platform to Generate Protein and Transcript Expression Data on the Single-Cell Level. *STAR protocols*.

57 Butler, A., Hoffman, P., Smibert, P., Papalexi, E. & Satija, R. Integrating single-cell transcriptomic data across different conditions, technologies, and species. *Nature biotechnology* **36**, 411-420, doi:10.1038/nbt.4096 (2018).

58 Amezquita, R. A. *et al.* Orchestrating single-cell analysis with Bioconductor. *Nature Methods* **12**, 1-9, doi:10.1038/s41592-019-0654-x (2019).

Figure legends:

Fig. 1: The immune phenotypes in inflamed non-malignant OM tissues largely resemble those of HNSCC tumors.

(a) Overview of experimental strategy. OM: inflamed oral mucosal tissue samples from routine dental surgeries. HNSCC: head and neck squamous cell carcinoma (primarily from the oral and oropharyngeal cavity) tissues from treatment-naive patients after surgical resection.

(b) Representative plots and quantification for the tissue residency markers CD69 and CD103 on CD8+ T cells from peripheral blood (blue), OM (orange) and HNSCC (red). (c) Representative plots and quantification for PD-1 expression on CD8+ T cells. (d) Heatmap showing the expression pattern for all the indicated molecules within CD8+ cytotoxic T cells (left) and CD4+ helper T cells (without Tregs, right) across peripheral blood, OM, and HNSCC. (e) Quantification of the indicated antigen-presenting cell (APC) populations. (f) Representative histograms and quantification for CD206, CD163 and CX3CR1 on CD14+ cells. (g) Heatmap representing the expression pattern for all the indicated molecules within CD1c+ cDC2s/DC3s (top) and CD14+ cells (bottom). All summary graphs are represented as mean ± SD (n=12 for OM and n=13 for HNSCC samples for T cell data, n = 16 for OM and HNSCC for APC data). Statistical analyses were performed using one-way ANOVA with Tukey's multiple comparisons test.

Fig. 2: Comprehensive single-cell RNA-seq analysis of OM and HNSCC immune infiltrates reveals subset-specific cytokine modules in the APC compartment.

(a) UMAP plots of the combined scRNA-seq data after Harmony integration, colored by donor (left) and by cell annotation (right).
(b) UMAP plot colored by tissue origin of the cells. (c) UMAP plot of the APC populations, colored by cluster and showing key differentially expressed genes per cluster on a z-score normalized heatmap (right). (d) Relative cluster abundance. (e) Relative contribution of each tissue source to the indicated cluster. (f) Dot Plot showing the transcript expression across myeloid clusters from combined OM+HNSCC data. (g) Number of DE genes between HNSCC and OM-derived cells per cluster. (h) Violin Plots showing the expression of key molecules for the DC3 cluster (left) and the cDC1 cluster (right).
All graphs are showing combined data for n=4 for OM samples, n = 4 for HNSCC samples, with a total of 140.764 cells after QC.

Fig. 3: NicheNet analysis predicts tumor-unique T cell specific crosstalk between tumor-infiltrating APCs and T cells.

(a) Simplified overview of the utilized NicheNet workflow. NicheNet was applied to the scRNA-seq data shown in Fig. 2 (only OM/HNSCC-derived cells utilized, w/o pDCs and mast cells). (b) Circos plots showing the top 20 ligand-receptor pairs identified by NicheNet for the indicated T cell subsets. Transparency of the connection represents the interaction strength. APC ligands are on the bottom, T cell receptors on top. (c) Representative plots showing the expression for the cytokines IL-1a and IL-1b after ex vivo culture in the presence of Brefeldin A. (d) Concentration of IL-1a and IL-1b and IL-18 as measured by Luminex analysis in flash-frozen HNSCC samples. LOD: limit of

detection. (e) Representative plots and quantification for the expression IL-1R1 on the indicated T cell subsets.

(f) Representative plots showing the expression of ICOS, HLA-DR, IL-18R1 and the chemokine receptor CXCR6 on the indicated T cell subsets from HNSCC. (g) Representative plots showing that within total CD45+ live hematopoietic cells in HNSCC, the majority of the ICOS+ IL1R1+ cell fraction falls within the CD4+ CD25+ CD127- Treg gate.

All summary graphs are represented as mean ± SD, n=4 for Luminex data, and n=6 for flow cytometry data.

Fig. 4: IL-1R1-expressing Tregs represent a functionally distinct Treg population with hallmarks of recent TCR stimulation.

(a) UMAP plot of Tregs sorted from blood and tumor of three different HNSCC donors after performing targeted transcriptomics, colored by cluster. (b) Violin plots showing the expression of selected transcripts across Treg clusters in HNSCC. (c) UMAP plot of tumor-infiltrating T cells from two HNSCC donors after performing short-term stimulation and targeted transcriptomics with AbSeq. Cells are colored by cluster, heatmaps show top differentially expressed proteins (top) and transcripts (bottom) across the indicated clusters. (d) CD40L and CTLA4 expression by CD4+ T cells (bottom) and Tregs after short-term stimulation with PMA/Ionomcyin. (e) ICOS and IL-1R1 surface protein expression on CTLA4+ (red) and CTLA4- (grey) Tregs after stimulation. (f) IL-1R1, PD-1 and IL-1R2 expression on sorted Tregs from peripheral

524 blood of healthy donors (blue) and tumor tissue (grey and red) cultured unstimulated or
525 in the presence of anti-CD3/28 beads for 2 days.
526 All summary graphs are represented as mean ± SD (total n=5 for scRNA-seq data, n=3
527 for stimulation assay) Statistical analyses were performed using one-way ANOVA with
528 Tukey's multiple comparisons test.
529

Methods:

Primary cells:

The head and neck squamous cell carcinoma (HNSCC) tissue samples were obtained after informed consent from otherwise treatment-naïve patients undergoing surgical resection of their primary tumor, ensuring that the immune infiltrate was not influenced by prior therapeutic interventions such as radiotherapy. Inflamed oral tissue biopsies were obtained from individuals undergoing routine dental surgeries for a variety of inflammatory conditions such as periimplantitis, periodontitis or osseous surgery. Matched peripheral blood samples were collected from each tissue donor. All study participants signed a written informed consent before inclusion in the study, and the protocols were approved by the institutional review board (IRB) at the Fred Hutchinson Cancer Research Center (IRB#6007-972 and IRB#8335). A detailed list of the samples and relevant procedure information is provided in Suppl table 1. Furthermore, cryopreserved peripheral blood mononuclear cells (PBMCs) from healthy controls (Seattle Area Control Cohort) were obtained via the HIV Vaccine Trial network (HVTN) and used for titrations, panel development and as a longitudinal technical control for all flow cytometry acquisitions.

Isolation of leukocytes from solid human tissues and peripheral blood:

After surgical procedures, fresh tissue samples were placed immediately into a 50ml conical tube with complete media (RPMI1640 supplemented with Penicillin, Streptomcyin and 10% Fetal Bovine Serum (FBS)) and kept at 4°C. Samples were

processed within 1-4 hours after collection based on optimized protocols adapted from (Leelatian et al., 2017). Briefly, tissue pieces were minced using a scalpel into small pieces and incubated with Collagenase II (Sigma-Aldrich, 0.7 mg/ml) and DNAse (50000 Units/ml) in RPMI1640 with 7.5% FBS for 30-45 minutes depending on sample size. Subsequently, any remaining tissue pieces were mechanically disrupted by repeated resuspension with a 30ml syringe with a large bore tip (16x1 ½ blunt). The cell suspension was filtered using a 70um cell strainer, washed in RPMI1640 and immediately used for downstream procedures.

Peripheral blood samples (1-10 ml) were collected in ACD tubes and then processed using SepMate tubes (StemCell Technologies, #85450) and Lymphoprep (Stem Cell Technologies, #07851) according to manufacturer protocols. Briefly, whole blood samples were centrifuged for 10 minutes at 400g, and the plasma supernatant was collected separately and immediately frozen at -80°C. Remaining cells were resuspended in 30ml of PBS and pipetted on top of 13.5ml Lymphoprep in a SepMate tube. After centrifugation for 16 minutes at 1200g, the mononuclear cell fraction in the supernatant was poured into a fresh 50ml tube, washed with PBS and immediately used for downstream procedures.

If required, cells isolated from tissue samples or from peripheral blood were frozen using either a 90%FBS/10%DMSO mixture or Cell Culture Freezing Medium (Gibco, #12648010), and stored in liquid nitrogen.

Flow Cytometry and Cell sorting:

For flow cytometric analysis good practices were followed as outlined in the guidelines for use of flow cytometry [53]. Directly following isolation, cells were incubated with Fc-blocking reagent (BioLegend Trustain FcX, #422302) and fixable UV Blue Live/Dead reagent (ThermoFisher, #L34961) in PBS (Gibco, #14190250) for 15 minutes at room temperature. After this, cells were incubated for 20 minutes at room temperature with 50 μl total volume of antibody master mix freshly prepared in Brilliant staining buffer (BD Bioscience, #563794), followed by two washes. All antibodies were titrated and used at optimal dilution, and staining procedures were performed in 96-well round-bottom plates (for cell sorting in 5ml polystyrene tubes). A detailed list of the main panels used, including fluorochromes, antibody catalogue numbers and final dilutions is provided in Suppl table 2 (panels designed according to best practices as described in [54]). For sorting cells were immediately used after staining, and for analysis, the stained cells were fixed with 4% PFA (Cytofix/Cytoperm, BD Biosciences) for 20 minutes at room temperature, washed, resuspended in FACS buffer and stored at 4°C in the dark until acquisition. If necessary, intracellular (CD68, Granzyme B) or intranuclear staining (Foxp3, KI67) was performed following the appropriate manufacturer protocols (eBioscience Foxp3/Transcription Factor Staining Buffer Set, Thermo Fisher #00-5532-00)

Single-stained controls were prepared with every experiment using antibody capture beads diluted in FACS buffer (BD Biosciences anti-mouse, #552843 or anti-mouse Plus, and anti-rat, #552844), or cells for Live/Dead reagent, and treated exactly the same as the samples (including fixation procedures). For each staining of experimental

599 samples, a PBMC sample from the same healthy donor was stained with the same
600 panel as a longitudinal reference control.
601 All samples were acquired using a FACSymphony A5 (BD Biosciences), equipped with
602 30 detectors and 355nm (65mW), 405nm (200mW), 488nm (200mW), 532nm (200mW)
603 and 628nm (200mW) lasers and FACSDiva acquisition software (BD Biosciences).
604 Detector voltages were optimized using a modified voltage titration approach [55] and
605 standardized from day to day using MFI target values and 6-peak Ultra Rainbow Beads
606 (Spherotec, # URCP-38-2K) [54]. After acquisition, data was exported in FCS 3.1 format
607 and analyzed using FlowJo (version 10.6.x, and 10.7.x, BD Biosciences). Samples were
608 analyzed using a combination of manual gating and computational analyses
609 approaches, with doublets being excluded by FSC-A vs FSC-H gating, and. For
610 samples acquired on different experimental days, files were exported as compensated
611 data and analyzed combined together in a new workspace. Gates were kept the same
612 across all samples except where changes in the density distribution clearly indicated
613 the need for adjustment. For the APC panel, PD-L1 (V450 channel) was excluded from
614 analysis because of interference from highly auto-fluorescent myeloid cells in some
615 samples.
616 All cell sorting was performed either on a FACSAria III (BD Biosciences), equipped with
617 20 detectors and 405nm, 488nm, 532nm and 628nm lasers or on a FACSymphony S6
618 cells sorter (BD Biosciences), equipped with 50 detectors and 355nm, 405nm, 488nm,
619 532nm and 628nm lasers. For all sorts involving myeloid cells, an 85 μm nozzle
620 operated at 45 psi sheath pressure was used, for sorts exclusively targeting T cells, a
621 70 μm nozzle at 70 psi sheath pressure was used. Cells were sorted into chilled

Eppendorf tubes containing 500-1000 μL of complete RPMI, washed once in PBS and immediately used for subsequent processing.

Whole Transcriptome single-cell library preparation and sequencing:

cDNA libraries were generated using the 10x Genomics Chromium Single Cell 3' Reagent Kits v2 protocol or the v3 protocol (10x Genomics). Briefly, after sorting single cells were isolated into oil emulsion droplets with barcoded gel beads and reverse transcriptase mix using the Chromium controller (10x Genomics). cDNA was generated within these droplets, then the droplets were dissociated. cDNA was purified using DynaBeads MyOne Silane magnetic beads (ThermoFisher, #370002D). cDNA amplification was performed by PCR (10 cycles) using reagents within the Chromium Single Cell 3' Reagent Kit v2 or v3 (10x Genomics) (see Suppl. Table 1). Amplified cDNA was purified using SPRIselect magnetic beads (Beckman Coulter). cDNA was enzymatically fragmented and size selected prior to library construction. Libraries were constructed by performing end repair, A-tailing, adaptor ligation, and PCR (12 cycles). Quality of the libraries was assessed by using Agilent 2200 TapeStation with High Sensitivity D5000 ScreenTape (Agilent). Quantity of libraries was assessed by performing digital droplet PCR (ddPCR) with Library Quantification Kit for Illumina TruSeq (BioRad, #1863040). Libraries were diluted to 2 nM or 3 nM and paired-end sequencing was performed on a HiSeq 2500 (Illumina) or a NovaSeq 6000 (Illumina).

Targeted transcriptomics single-cell library preparation and sequencing:

cDNA libraries were generated as described in detail in the following protocol [56]. Briefly, after sorting single cells were stained with Sample-Tag antibodies (if required), washed, pooled and counted and subsequently loaded onto a nano-well cartridge (BD Rhapsody), lysed inside the wells followed by mRNA capture on cell capture beads according to manufacturer instructions. Cell Capture Beads were retrieved and washed prior to performing reverse transcription and treatment with Exonuclease I. cDNA underwent targeted amplification using the Human Immune Response Panel primers and a custom supplemental panel (listed in Suppl Table 3) via PCR (10-11 cycles). PCR products were purified, and mRNA PCR products were separated from Sample-Tag (and AbSeq, where applicable) PCR products with double-sided size selection using SPRIselect magnetic beads (Beckman Coulter). mRNA and Sample Tag products were further amplified using PCR (10 cycles). PCR products were then purified using SPRIselect magnetic beads. Quality of PCR products was determined by using an Agilent 2200 TapeStation with High Sensitivity D5000 ScreenTape (Agilent) in the Fred Hutch Genomics Shared Resource laboratory. Quantity of PCR products was determined by Qubit with Qubit dsDNA HS Assay (#Q32851). Targeted mRNA product was diluted to 2.5 ng/μL, and the Sample Tag and AbSeq PCR products were diluted to 1 ng/μL to prepare final libraries. Final libraries were indexed using PCR (6 cycles). Index PCR products were purified using SPRIselect magnetic beads. Quality of all final libraries was assessed by using Agilent 2200 TapeStation with High Sensitivity D5000 ScreenTape and quantified using a Qubit Fluorometer using the Qubit dsDNA HS Kit

(ThermoFisher). Final libraries were diluted to 3nM and multiplexed for paired-end (100bp) sequencing on NovaSeq 6000 (Illumina).

Ex vivo stimulation assays:

Cells were isolated from tumors or blood as described above. For some of the stimulation assays cryo-preserved cell suspensions were used. For the 2h short-term stimulation assays, $CD3^+$ T cells (live $CD45^+$ $CD19^-$ $CD3^+$ events) were isolated using Fluorescence-activated cell sorting (FACS) using a BD FACSAria II. 5,000 cells were placed into each well of a V-bottom 96-well plate with 200 ul complete media. Cells were then left untreated (control), or stimulated with IL-12/IL-15/IL-18 (each at 1nM), or with phorbol myristate acetate (PMA, 50ng/ml) and Ionomycin (Iono, 500ng/ml) for 2 hours at 37°C. Cells were then washed with 1xPBS and prepared for targeted transcriptomics and staining with oligo-conjugated antibodies as described above [56]. For the 2-day stimulation assays, $CD4^+$ $CD25^+$ $CD127^-$ Tregs were isolated using an BD S6 sorter, and cultured either in media alone or with anti-CD3/CD28 Dynabeads (Gibco, #11161D, used at a 1:1 bead-to-cell ratio). Prior to analysis,Dynabeads were removed using a magnet, and cells were staing for flow cytometric analysis as described above.

Luminex analysis of tumor lysates:

Luminex analysis was performed on lysates of tissues. To obtain lysates from tumor tissues, a 2x2mm piece was incubated for one minute in PBS/0.1% tween. After incubation, the tissue piece was minced in the buffer and then centrifuged at 10,000

rpm for 5 minutes. The supernatant was collected and immediately flash-frozen on dry ice. Processing for Luminex was performed by the Immunomonitoring Core of the Fred Hutchinson Cancer Research Center.

Pre-processing for WTA and targeted transcriptomics data:

Raw base call (BCL) files were demultiplexed to generate Fastq files using the cellranger mkfastq pipeline within Cell Ranger (10x Genomics). Whole transcriptome Fastq files were processed using the standard cellranger pipeline (10x genomics) within Cell Ranger 2.1.1 or Cell Ranger 3.0.2. Briefly, cellranger count performs read alignment, filtering, barcode and UMI counting, and determination of putative cells. The final output of cellranger (the molecule per cell count matrix) was then analyzed in R using the package Seurat (3.0) as described below. For targeted transcriptomics data, Fastq files were processed via the standard Rhapsody analysis pipeline (BD Biosciences) on Seven Bridges (www.sevenbridges.com). Briefly, after read filtering, reads are aligned to a reference genome and annotated, barcodes and UMIs are counted, followed by determining putative cells. The final output (molecule per cell count matrix) was also analyzed in R using Seurat (version 3.0) as described below.

Seurat workflow for targeted and WTA data:

The R package Seurat [57] was utilized for all downstream analysis, with custom scripts based on the following general guidelines for analysis of scRNA-seq data [58]. Briefly, for whole transcriptome data, only cells that had at least 200 genes (v2 kits) or 800 genes (v3 kits), and depending on sample distribution less than 7-15%

mitochondrial genes were included in analysis. All acquired samples were merged into a single Seurat object, followed by a natural log normalization using a scale factor of 10000, determination of variable genes using the vst method, and a z-score scaling. Principal component analysis (PCA) was used to generate 75 PCs, followed by data integration using Harmony [29]. The dimensionality reduction generated by Harmony was used to calculate UMAP, and graph-based clustering with a resolution between 0.2 and 0.6. For cell annotation, we applied SingleR as a purely data-driven approach [31], and used the expression of typical lineage transcripts to verify the cell label annotation. For all subsequent analysis steps, the integrated Seurat object was separated into two objects containing all T cells or all myeloid cells, respectively, and UMAP calculation as well as clustering steps were repeated.

For targeted transcriptomics data, separate cartridges from the same experiment were merged (if applicable), and only cells that had at least 30 genes were included in downstream analysis. After generating a Seurat object, a natural log normalization using a scale factor of 10000 was done, followed by determination of variable genes using the vst method, and a z-score scaling. PCA was used to generate 75 PCs, 30 of which were used for subsequent UMAP calculation and graph-based clustering with tuned resolution.

For all differential gene expression analysis we utilized the Seurat implementation of MAST (model-based analysis of single-cell transcriptomes) with the number of UMIs included as a covariate (proxy for cellular detection rate (CDR)) in the model [33].

NicheNet workflow:

NicheNet analysis was adapted from the vignette described on https://github.com/saeyslab/nichenetr [35]. Briefly, the separate Seurat objects containing T cells and APCs (described above) were subsetted to contain only OM and HNSCC derived cells. Different T cell subsets were set as "receiver" (i.e. CD4 non Treg clusters, CD8 T cell clusters and Treg clusters) and all myeloid cell clusters (except the pDC and mast cell cluster) as "sender" populations, respectively. For the receiver cell population, a DE gene test was performed to find genes enriched in HNSCC vs OM samples. NicheNet analysis was performed based on the vignette to infer receptors, filter for documented links and generate a circus plot of ligand-receptor interactions for the respective cellular populations.

Statistical analyses:

Unless stated otherwise, all data are represented as mean ± SD. Statistical analyses between blood, OM and HNSCC samples were performed using one-way ANOVA with Tukey's multiple comparisons test. * $P < 0.05$; ** $P < 0.01$; *** $P < 0.001$; **** $P < 0.0001$.

Code availability:

The sequencing data discussed in this publication have been deposited in the NCBI's Omnibus database at GEO-ID GSE163633, and the main scripts used for data processing are available on https://github.com/MairFlo.

Acknowledgements:

We thank the HIV Vaccine Trial Network (HVTN) for access to their flow cytometry instrumentation, the Flow Cytometry Shared Resources Core of the FHCRC, and the Genomics Shared Resources Core of the FHCRC for sequencing. We thank members of the Prlic lab for critical discussion, and Aaron J. Tyznik (BD Biosciences) for advice. This work was supported by NIH grants R01AI123323 (to M.P) and R21DE026565 (to M.P. and D.D) and the FHCRC President's Young Investigator Award (to M.P). F.M. is an ISAC Marylou scholar and was supported through The American Association of Immunologists (AAI) Intersect Fellowship Program for Computational Scientists and Immunologists. J.R.E. was supported by National Institutes of Health (NIH) T32 AI007509-20.

Author contributions:

Conceptualization: F.M, J.R.E and M.P.; Methodology: F.M, J.R.E, M.F., A.K.; Software: F.M., J.R.E, E.G, V.V; Formal Analysis: F.M., J.R.E, E.G, V.V, M.P.; Investigation: F.M, J.R.E, M.F.; Writing Original Draft: F.M, J.R.E and M.P.; Writing Review & Editing: F.M, J.R.E, M.F., E.G., V.V. D.D, B.B, R.G and M.P.; Visualization: F.M.; Funding Acquisition: D.D., R.G. and M.P; Resources: D.D and B.B.; Supervision: M.P.;

Competing interest declaration:

R.G. has received speaker fees from Illumina and Fluidigm and support from Juno Therapeutics and Janssen Pharma, has consulted for Takeda Vaccines, Juno

Therapeutics and Infotech Soft, and has ownership interest in CellSpace Bio. E.G. declares ownership interest in Ozette Technologies. F.M, J.R.E and M.P. are holding the related patent “Specific Targeting of Tumor-infiltrating regulatory T cells (Tregs) using ICOS and IL-1R1” (US patent #63/092957).

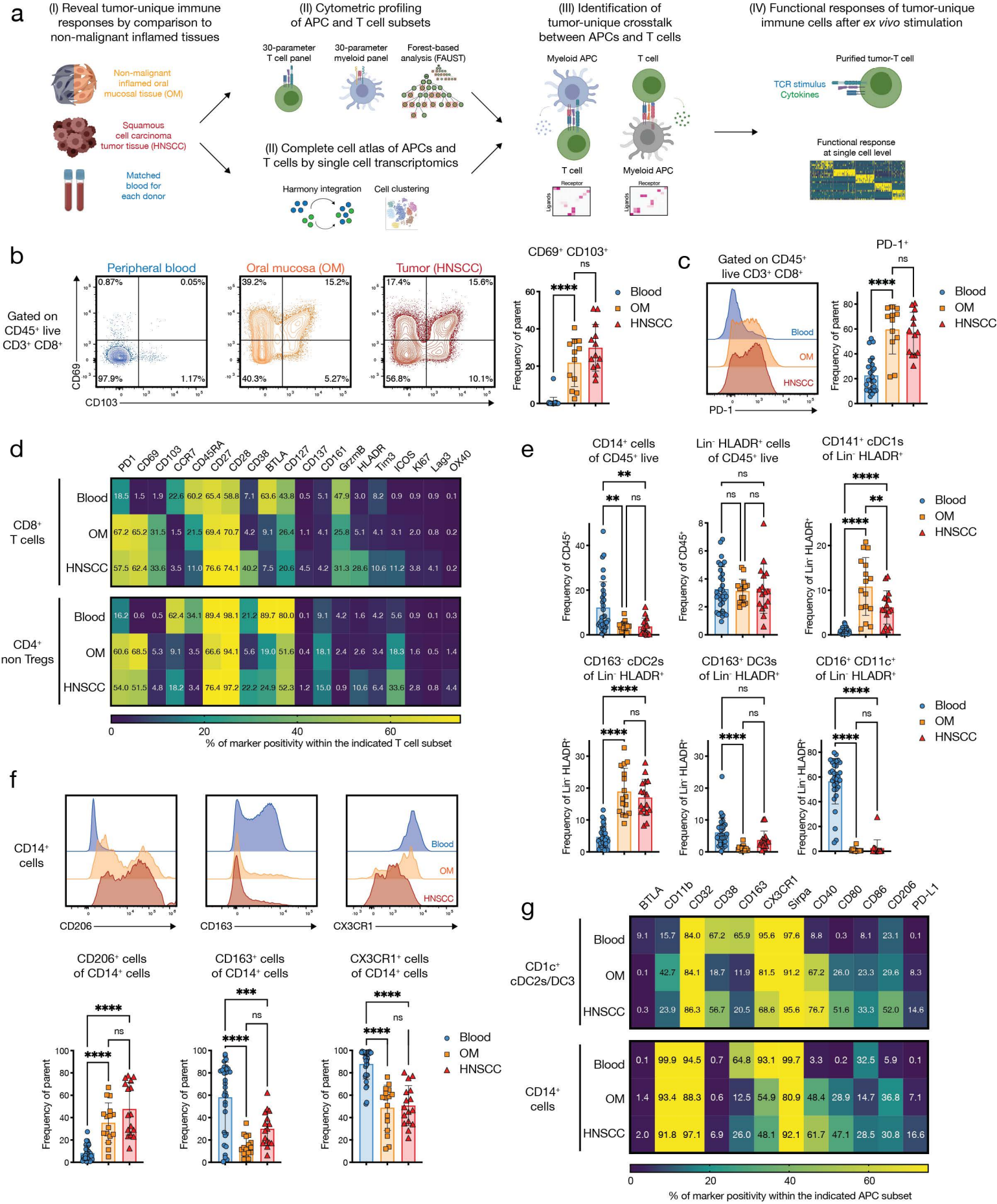

Fig. 1: The immune phenotypes in inflamed non-malignant OM tissues largely resemble those of HNSCC tumors.
(a) Overview of experimental strategy. OM: inflamed oral mucosal tissue samples from routine dental surgeries. HNSCC: head and neck squamous cell carcinoma (primarily from the oral and oropharyngeal cavity) tissues from treatment-naive patients after surgical resection. **(b)** Representative plots and quantification for the tissue residency markers CD69 and CD103 on CD8+ T cells from peripheral blood (blue), OM (orange) and HNSCC (red). **(c)** Representative plots and quantification for PD-1 expression on CD8+ T cells. **(d)** Heatmap showing the expression pattern for all the indicated molecules within CD8+ cytotoxic T cells (left) and CD4+ helper T cells (without Tregs, right) across peripheral blood, OM, and HNSCC. **(e)** Quantification of the indicated antigen-presenting cell (APC) populations. **(f)** Representative histograms and quantification for CD206, CD163 and CX3CR1 on CD14+ cells. **(g)** Heatmap representing the expression pattern for all the indicated molecules within CD1c+ cDC2s/DC3s (top) and CD14+ cells (bottom).
All summary graphs are represented as mean ± SD (n=12 for OM and n=13 for HNSCC samples for T cell data, n = 16 for OM and HNSCC for APC data). Statistical analyses were performed using one-way ANOVA with Tukey's multiple comparisons test.

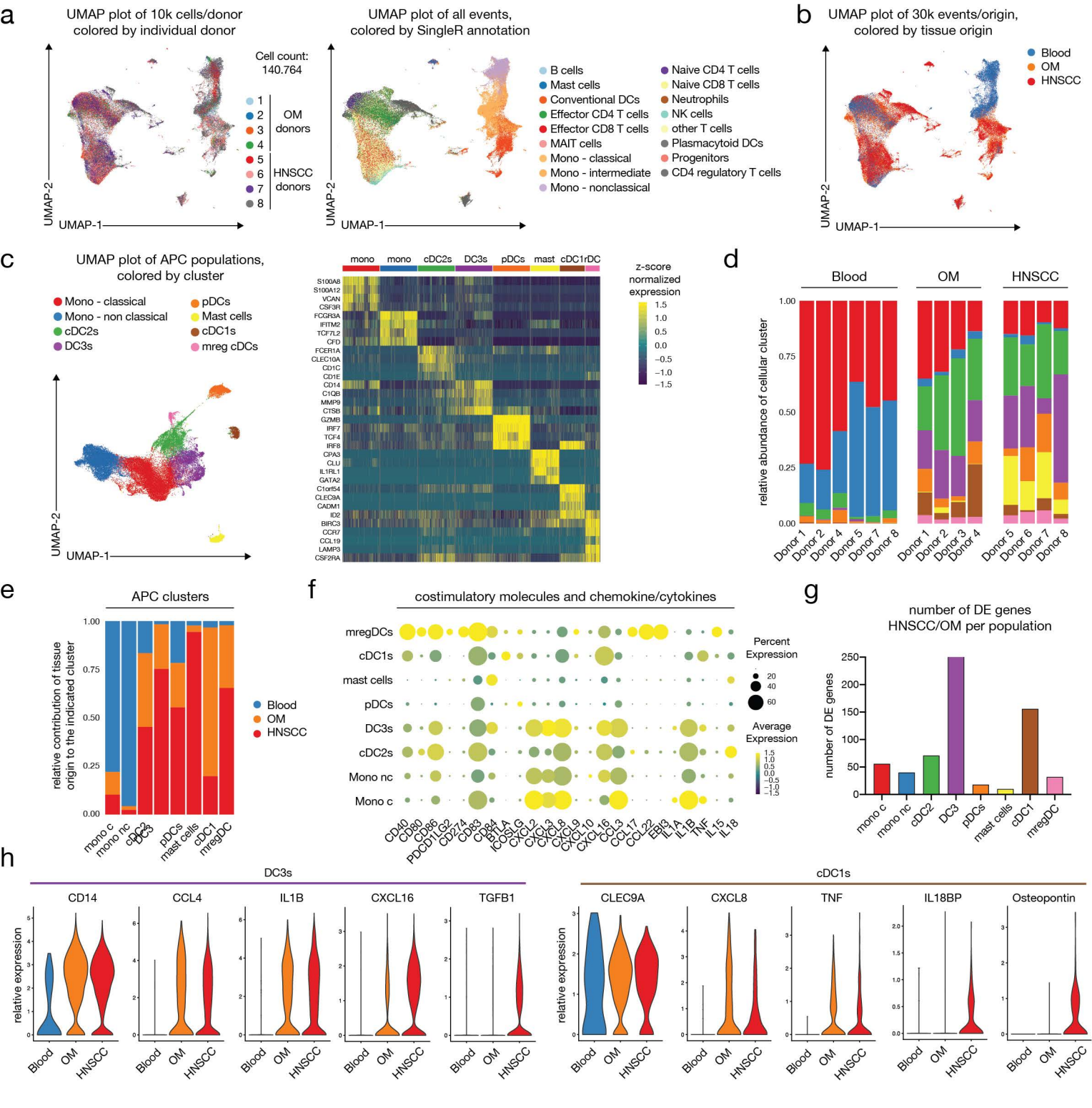

Fig. 2: Comprehensive single-cell RNA-seq analysis of OM and HNSCC immune infiltrates reveals subset-specific cytokine modules in the APC compartment.

(a) UMAP plots of the combined scRNA-seq data after Harmony integration, colored by donor (left) and by cell annotation (right). **(b)** UMAP plot colored by tissue origin of the cells. **(c)** UMAP plot of the APC populations, colored by cluster and showing key differentially expressed genes per cluster on a z-score normalized heatmap (right). **(d)** Relative cluster abundance. **(e)** Relative contribution of each tissue source to the indicated cluster. **(f)** Dot Plot showing the transcript expression across myeloid clusters from combined OM+HNSCC data. **(g)** Number of DE genes between HNSCC and OM-derived cells per cluster. **(h)** Violin Plots showing the expression of key molecules for the DC3 cluster (left) and the cDC1 cluster (right)

All graphs are showing combined data for n=4 for OM samples, n = 4 for HNSCC samples, with a total of 140.764 cells after QC.

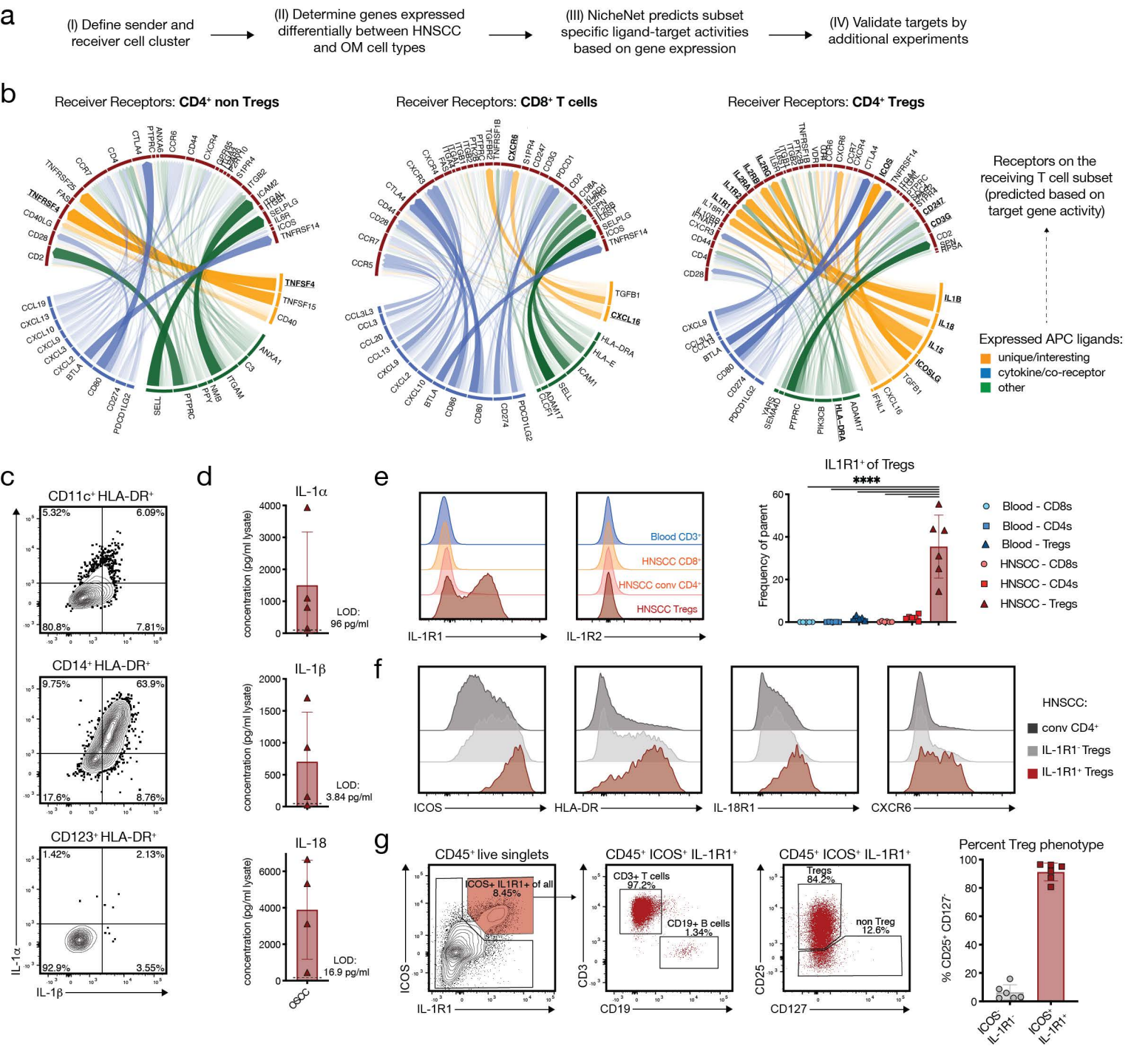

Fig. 3: NicheNet analysis predicts tumor-unique T cell specific crosstalk between tumor-infiltrating APCs and T cells.
(a) Simplified overview of the utilized NicheNet workflow. NicheNet was applied to the scRNA-seq data shown in Fig. 2 (only OM/HNSCC-derived cells utilized, w/o pDCs and mast cells). **(b)** Circos plots showing the top 20 ligand-receptor pairs identified by NicheNet for the indicated T cell subsets. Transparency of the connection represents the interaction strength. APC ligands are on the bottom, T cell receptors on top. **(c)** Representative plots showing the expression for the cytokines IL-1a and IL-1b after ex vivo culture in the presence of Brefeldin A. **(d)** Concentration of IL-1a and IL-1b and IL-18 as measured by Luminex analysis in flash-frozen HNSCC samples. LOD: limit of detection. **(e)** Representative plots and quantification for the expression IL-1R1 on the indicated T cell subsets. **(f)** Representative plots showing the expression of ICOS, HLA-DR, IL-18R1 and the chemokine receptor CXCR6 on the indicated T cell subsets from HNSCC. **(g)** Representative plots showing that within total CD45+ live hematopoietic cells in HNSCC, the majority of the ICOS+ IL1R1+ cell fraction falls within the CD4+ CD25+ CD127- Treg gate.
All summary graphs are represented as mean ± SD, n=4 for Luminex data, and n=6 for flow cytometry data.

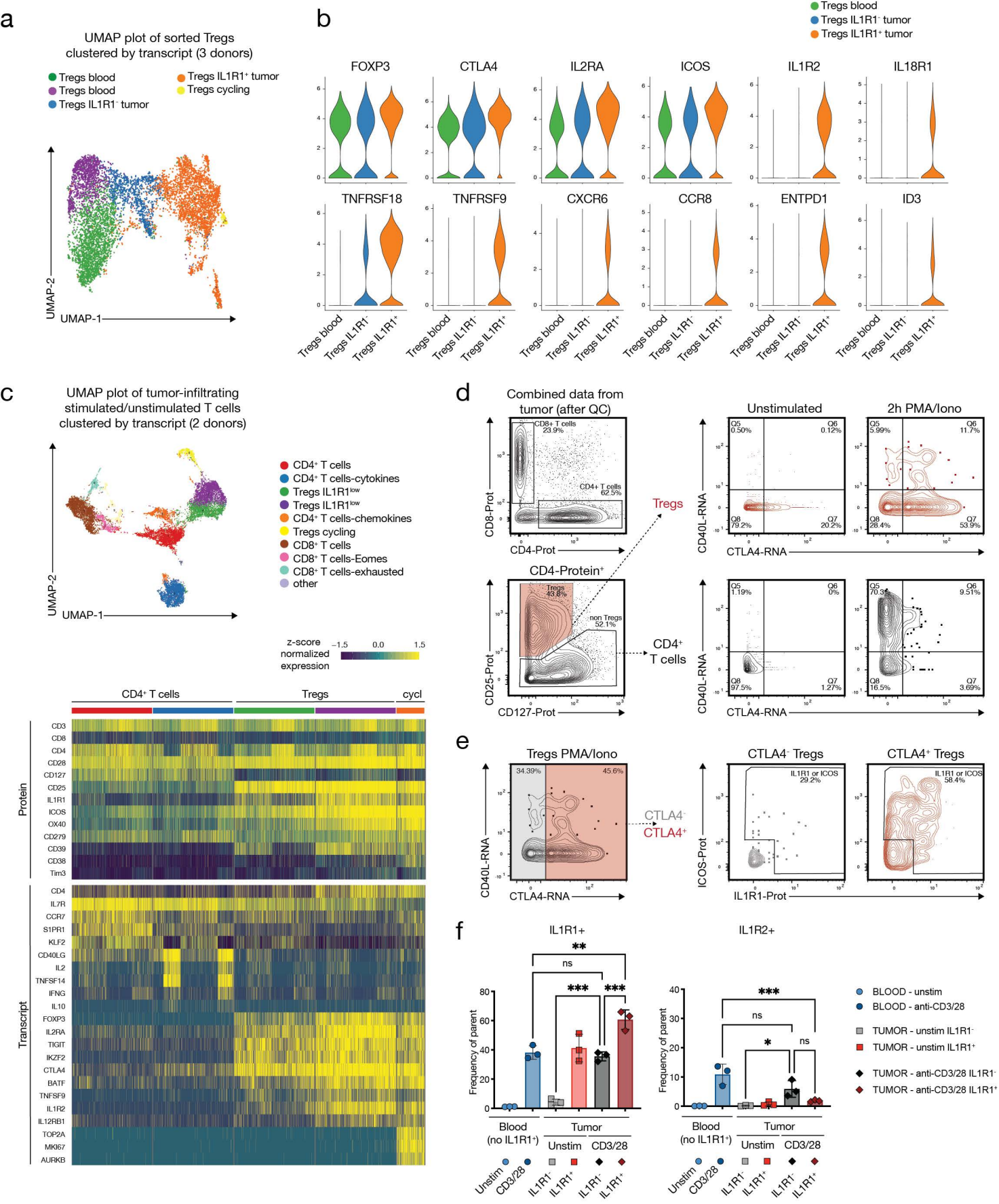

Fig. 4: IL-1R1-expressing Tregs represent a functionally distinct Treg population with hallmarks of recent TCR stimulation.
(a) UMAP plot of Tregs sorted from blood and tumor of three different HNSCC donors after performing targeted transcriptomics, colored by cluster. **(b)** Violin plots showing the expression of selected transcripts across Treg clusters in HNSCC. **(c)** UMAP plot of tumor-infiltrating T cells from two HNSCC donors after performing short-term stimulation and targeted transcriptomics with AbSeq. Cells are colored by cluster, heatmaps show top differentially expressed proteins (top) and transcripts (bottom) across the indicated clusters. **(d)** CD40L and CTLA4 expression by CD4+ T cells (bottom) and Tregs after short-term stimulation with PMA/Ionomcyin. **(e)** ICOS and IL-1R1 surface protein expression on CTLA4+ (red) and CTLA4- (grey) Tregs after stimulation. **(f)** IL-1R1 and IL-1R2 expression on sorted Tregs from peripheral blood of healthy donors (blue) and tumor tissue (grey and red) cultured unstimulated or in the presence of anti-CD3/28 beads for 2 days.
All summary graphs are represented as mean ± SD (total n=5 for scRNA-seq data, n=3 for stimulation assay) Statistical analyses were performed using one-way ANOVA with Tukey's multiple comparisons test.

Extended data Figure 1

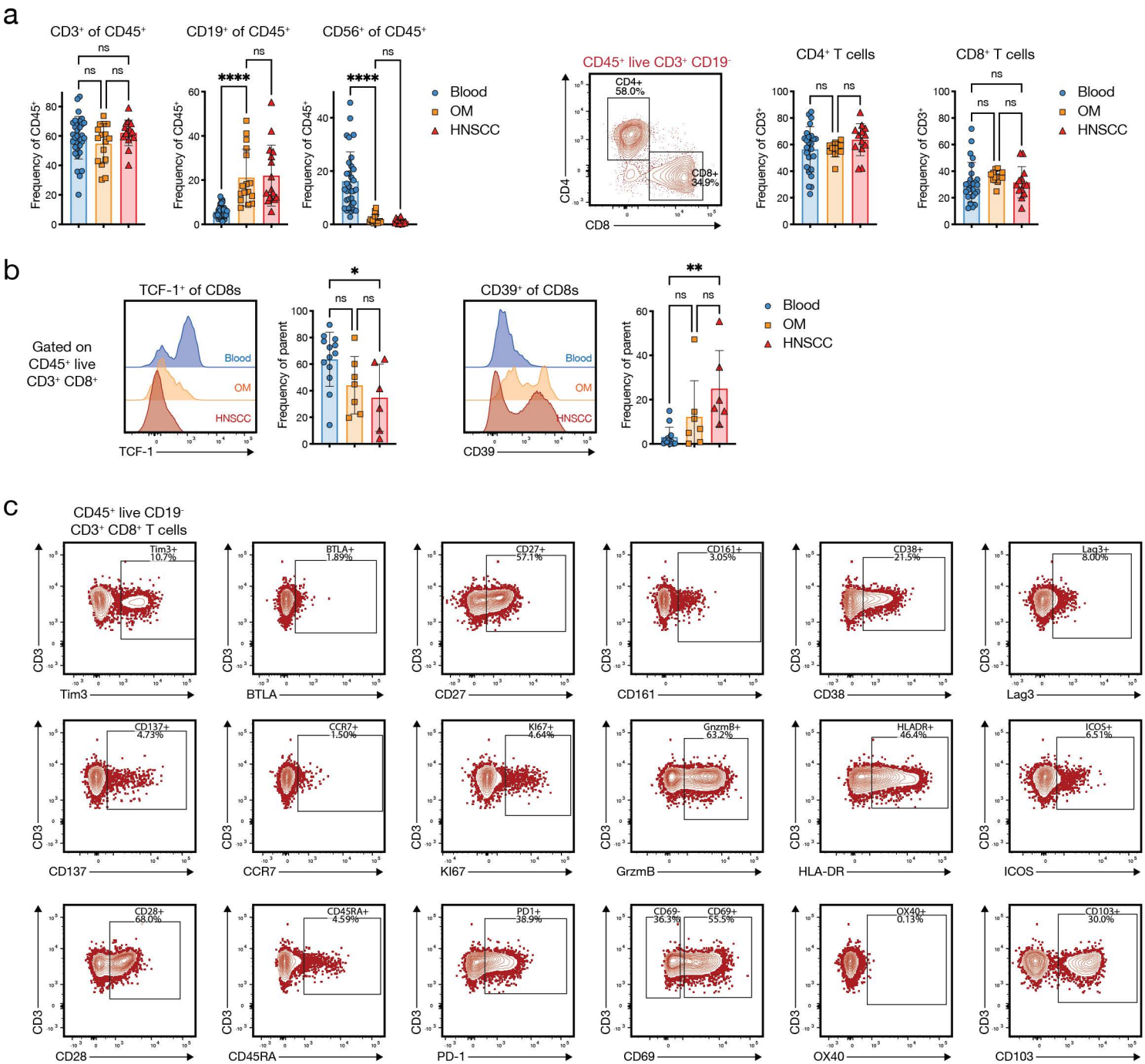

Extended data figure 1: Representative flow cytometry data for the 30-parameter APC panel.
(a) Quantification of CD3+ T cells, CD19+ B cells and CD56+ NK cells as well as the frequency of CD4+ and CD8+ T cells.
(b) Representative histograms and quantification for the expression for the transcription factor TCF-1 (left, n=6) and CD39 (right, n=6) on CD8+ T cells.
(c) Staining patterns for all phenotyping markers in the high-dimensional T cell panel shown on a representative HNSCC sample, pregated on live CD8+ T cells.

Extended data Figure 2

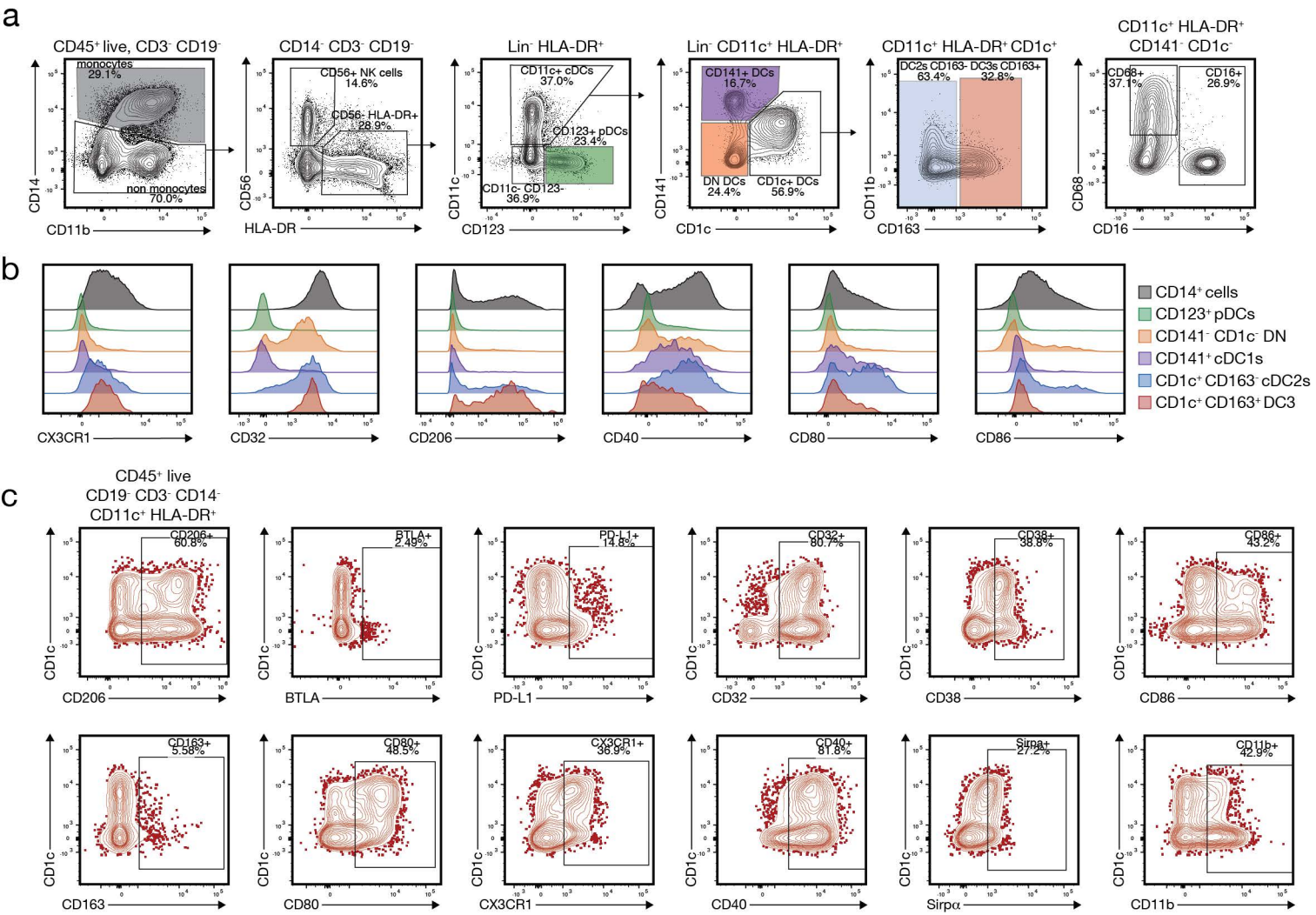

Extended data figure 2: Representative flow cytometry data for the 30-parameter APC panel.
(a) Representative gating strategy for the identification of canonical antigen-presenting cells (APCs) in HNSCC. Plots are concatenated from three individual donors. Color coding of gates refers to the populations used for histograms in (b).
(b) Staining patterns for all phenotyping markers in the high-dimensional myeloid APC panel shown on a representative HNSCC sample, pregated on live pan CD11c$^+$ HLA-DR$^+$ conventional DCs.
(c) Staining patterns for all phenotyping markers in the high-dimensional myeloid APC panel shown on a representative HNSCC sample, pregated on live pan CD11c$^+$ HLA-DR$^+$ conventional DCs.

Extended data Figure 3

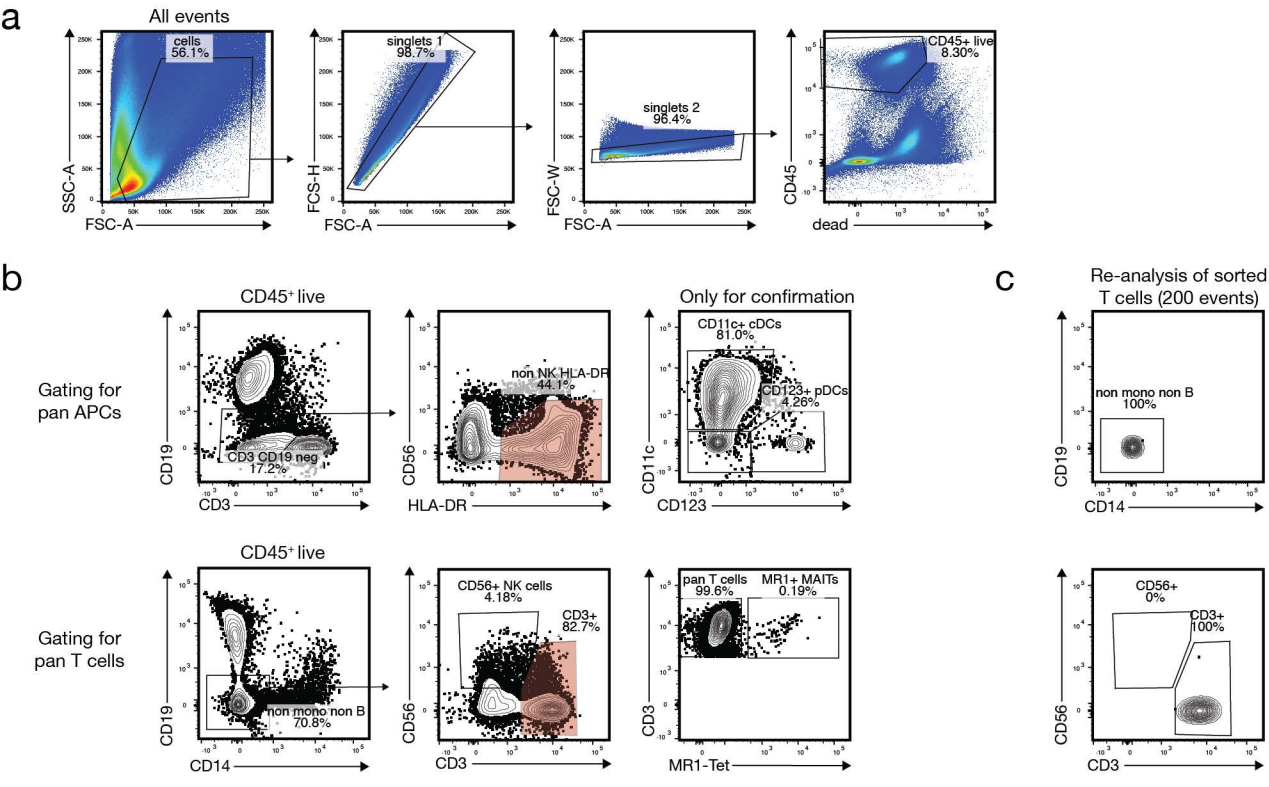

Extended data Figure 3: Gating strategy used for WTA (10x) scRNA-seq sorts.
(a) General gating of a representative OM tissue sample for CD45⁺ live events.
(b) Gating trees used for sorting the pan APC population and for pan T cells. Red shaded gates were sorted. CD11c and CD123 staining was only used to verify presence of cDCs and pDCs in the respective sample. For some experiments (data not shown) MR1-Tetramer⁺ mucosal associated invariant T cells (MAIT cells) and CD56⁺ NK cells were sorted separately.
(c) Re-analysis of a fraction of sorted pan T cells.

Supplementary Table 1
List of tissue types analyzed

Type	ID	Tissue source	Infl Score	APC panel	T cell panel	IL1R1 panel	sc-RNAseq
OM	116	dental: sulcular and attached gingiva	High	Yes			
OM	119	dental: sulcular and attached gingiva	Low	Yes	Yes		
OM	121	implant: sulcular and attached gingiva	High				10x v2
OM	122	dental: sulcular and attached gingiva	Low				10x v2
OM	124	dental: sulcular and attached gingiva	High				10x v2
OM	125	dental: sulcular and attached gingiva	High				10x v2
OM	127	dental: sulcular and attached gingiva	High	Yes	Yes		
OM	128	dental: sulcular and attached gingiva	High	Yes	Yes		
OM	136	dental: sulcular and attached gingiva	High	Yes			
OM	138	dental: sulcular and attached gingiva	Low	Yes	Yes		
OM	139	dental: sulcular and attached gingiva	Low	Yes	Yes		
OM	141	dental: sulcular and attached gingiva	Low	Yes	Yes		
OM	145	dental: sulcular and attached gingiva	Low	Yes			
OM	152	dental: sulcular and attached gingiva	NA	Yes	Yes		
OM	153	implant: sulcular and attached gingiva	Low	Yes	Yes		
OM	161	dental: sulcular and attached gingiva	Low		Yes		
OM	162	dental: sulcular and attached gingiva	NA	Yes	Yes		
OM	163	dental: sulcular and attached gingiva	NA	Yes	Yes		
OM	167	implant: sulcular and attached gingiva	High	Yes			
OM	169	dental: sulcular and attached gingiva	Low	Yes	Yes		
OM	170	implant: sulcular and attached gingiva	Low	Yes			
Type	**ID**	**Tissue source**	**Infl Score**	**APC panel**	**T cell panel**	**IL1R1 panel**	**sc-RNAseq**
HNSCC	2	base of tongue SCC	NA				10x v2
HNSCC	4	base of tongue SCC	NA	Yes	Yes		Rhaps
HNSCC	6	oral tongue SCC	NA	Yes	Yes		
HNSCC	7	oral tongue SCC	NA	Yes	Yes		Rhaps
HNSCC	7b	tonsil SCC	NA	Yes	Yes		
HNSCC	8	oral tongue SCC	NA	Yes	Yes		Rhaps
HNSCC	11	tonsil SCC	NA	Yes	Yes		
HNSCC	12	tonsil SCC	NA	Yes	Yes		
HNSCC	13	oral tongue SCC	NA				Rhaps+AbSeq
HNSCC	14	laryngeal SCC	NA	Yes	Yes		Rhaps+AbSeq
HNSCC	15	oral tongue SCC	NA	Yes	Yes		10x v2
HNSCC	17	tonsil SCC	NA	Yes			
HNSCC	18	metastatic SCC to cervical lymph node	NA	Yes	Yes		Rhaps+AbSeq

HNSCC	19	base of tongue SCC	NA	Yes	Yes		
HNSCC	20	base of tongue SCC	NA				10x v3
HNSCC	21	maxillary sinus SCC	NA	Yes			
HNSCC	22	metastatic SCC to cervical lymph node	NA		Yes		
HNSCC	23	tonsil SCC	NA			Yes	
HNSCC	27	laryngeal SCC	NA	Yes	Yes		10x v3
HNSCC	28	palatal lesion SCC	NA			Yes	
HNSCC	29	floor of mouth SCC	NA			Yes	
HNSCC	30	oral tongue SCC	NA	Yes	Yes		
HNSCC	35	base of tongue SCC	NA	Yes			
HNSCC	43	metastatic SCC to cervical lymph node	NA	No	No	Yes	
HNSCC	48	oral tongue SCC	NA	No	No	Yes	
HNSCC	49	base of tongue	NA				Rhaps+AbSeq
HNSCC	51	oral tongue SCC	NA				Rhaps+AbSeq
HNSCC	53	base of tongue SCC	NA			Yes	

Supplementary Table 2

High-dimensional flow cytometry panels and antibodies

For development and details, see Mair et al, Cytometry Part A2018

For clones and ordering numbers, see antibody table
ic: marker stained intracellularly after fixation
and permeabilization

PANEL 1: APC panel

		Flourophore	Antigen	Dilutions
1	355nm	BUV395	CD40	1: 40
2		Violet L/D	L/D	1: 500
3		BUV496	CD16	1: 320
4		BUV563	CD56	1: 160
5		BUV661	CD3	1: 80
6		BUV737	CD86	1: 40
7		BUV805	CD45	1: 80
8	405nm	BV421	PD-L2	1: 20
9		BV480	CD85k	1: 40
10		BV570	CD14	1: 20
11		BV605	CD141	1: 640
12		BV650	Sirpa	1: 160
13		BV711	*CD68*	*1: 40* *ic*
14		BV750	CD11b	1: 160
15		BV785	CD123	1: 40
16	488nm	BB515	CD206	1: 20
17		BB630	BTLA	1: 80
18		BB660	PD-L1	1: 40
19		BB700	CD32	1: 160
20		BB790	CD38	1: 80
21	532nm	PE	Axl	1: 20
22		PE-CF594	CD163	1: 40
23		PE-Cy5	CD80	1: 10
24		PE-Cy5.5	CD19	1: 160
25		PE-Cy7	CX3CR1	1: 160
26	628nm	AF647	CD1c	1: 160
27		AF700	CD11c	1: 320
28		APC-H7	HLA-DR	1: 40

PANEL 2: general T cell panel

		Flourophore	Antigen	Dilutions
1	355nm	BUV395	CD8	1: 80
2		Violet L/D	L/D	1: 500
3		BUV496	CD3	1: 40
4		BUV563	CD25	1: 40
5		BUV661	HLA-DR	1: 80
6		BUV737	ICOS	1: 10
7		BUV805	CD45	1: 80
8	405nm	BV421	MR1Tet	1: 500
9		BV480	CD28	1: 40
10		BV570	CD45RA	1: 160
11		BV605	PD1	1: 20
12		BV650	CD69	1: 20
13		BV711	OX40	1: 40
14		BV750	CD103	1: 160
15		BV785	IL7Ra	1: 10
16	488nm	BB515	Tim3	1: 80
17		BB630	BTLA	1: 80
18		BB660	CD27	1: 160
19		BB700	CD161	1: 20
20		BB790	CD38	1: 80
21	532nm	PE	Lag3	1: 20
22		PE-CF594	TCRgd	1: 20
23		PE-Cy5	CD137	1: 20
24		PE-Cy5.5	CD19	1: 160
25		PE-Cy7	CCR7	1: 40
26	628nm	eFlour660	*KI67*	1: *1000*
27		AF700	*GrzmB*	*1: 80*
28		APC-H7	CD4	1: 40

PANEL 3: Transcription factor panel

		Flourophore	Antigen	Dilutions
1	355nm	BUV395	CD8	1: 80
2		Violet L/D	dead	1: 500
3		BUV496	CD3	1: 40
4		BUV563	CD25	1: 40
5		BUV661	TCRgd	1: 40
6		BUV737	CD69	1: 80

PANEL 4: IL1R1/chemokine panel

		Flourophore	Antigen	Dilutions
1	355nm	BUV395	CD8	1: 80
2		Violet L/D	L/D	1: 500
3		BUV496	CD3	1: 40
4		BUV563	CXCR6	1: 20
5		BUV661	CCR7	1: 80
6		BUV737	ICOS	1: 20

7		BUV805	CD45	1: 80		7		BUV805	CD45	1: 80		
8	405nm	BV421	MR1-Tet	1: 500		8	405nm	BV421	CD25	1: 40		
9		BV510	CCR7	1: 10		9		BV480	CD28	1: 40		
10		BV570	CD45RO	1: 20		10		BV570	CD45RA	1: 160		
11		BV605	CD39	1: 20		11		BV605	CD39	1: 40		
12		BV650	Tim3	1: 20		12		BV650	CD69	1: 20		
13		BV711	CCR5	1: 20		13		BV711	CCR8	1: 20		
14		BV750	CD103	1: 160		14		BV750	CD103	1: 160		
15		BV786	*KI-67*	1: 320	*ic*	15		BV785	CCR5	1: 20		
16	488nm	BB515	CD45RA	1: 40		16	488nm	BB515	Tim3	1: 80		
17		BB630	*CTLA-4*	1: 80	*ic*	17		BB630	BTLA	1: 80		
18		BB660	CD127	1: 40		18		BB660	CD127	1: 20		
19		BB700	PD1	1: 20		19		BB700	PD1	1: 20		
20		BB790	TIGIT	1: 80		20		BB790	TIGIT	1: 40		
21	532nm	PE	*TCF-7*	1: 40	*ic*	21	532nm	PE	IL-1R1	1: 20		
22		PE-eFlo610	*EOMES*	1: 10	*ic*	22		PE-CF594	CXCR3	1: 20		
23		PE-Cy5	CD137	1: 20		23		PE-Cy5	CD137	1: 20		
24		PE-Cy5.5	*Foxp3*	1: 10	*ic*	24		PE-Cy5.5	CD19	1: 160		
25		PE-Cy7	*Tbet*	1: 20	*ic*	25		PE-Cy7	IL18R1	1: 40		
26	628nm	APC	*Tox*	1: *80*	*ic*	26	628nm	APC	IL-1R2	1: *20*		
27		AF700	*GrzmB*	*1: 80*	*ic*	27		AF700	HLA-DR	*1: 160*		
28		APC-H7	*CD4*	1: 40		28		APC-H7	CD4	1: 40		

Antibody table	**Company**	**Cat.no/Identifier**
CD183 (CXCR3)-PE-CF594 (clone 1C6)	BD Biosciences	Cat#562451; RRID:AB_11153118
CD3-BUV496 (clone UCHT1)	BD Biosciences	Cat#564809; RRID:AB_2744388
CD3-BUV661 (clone UCHT1)	BD Biosciences	Cat#612964; RRID:AB_2870239
CD25-BV421 (clone 2A3)	BD Biosciences	Cat#564033; RRID:AB_2738555
CD25-BUV563 (clone 2A3)	BD Biosciences	Cat#612918; RRID:AB_2870203
HLA-DR-BUV661 (cloneG46-6)	BD Biosciences	Cat#612980; RRID:AB_2870252
ICOS-BUV737 (clone DX29)	BD Biosciences	Cat#749665; RRID:AB_2873929
CD8-BUV395 (clone RPA-T8)	BD Biosciences	Cat#563795; RRID:AB_2722501
TCRgd-PE-CF594 (clone B1)	BD Biosciences	Cat#562511; RRID:AB_2737631
CD14-BV570 (clone M5E2)	BioLegend	Cat#301832; RRID:AB_2563629
PD1-BB700 (clone EH12.1)	BD Biosciences	Cat#566460; RRID:AB_2744348
PD1-BV605 (clone EH12.1)	BD Biosciences	Cat#563245; RRID:AB_2738091
CD69-BV650 (clone FN50)	BD Biosciences	Cat#563835; RRID:AB_2738442
CD45RA-BV570 (clone HI100)	BioLegend	Cat#304132; RRID:AB_2563813
CD103-BV750 (clone Ber-ACT8)	BD Biosciences	Cat#747099; RRID:AB_2871852
CD127-Biotin (A019D5)	BioLegend	Cat#351346; RRID:AB_2566509
CD127-BV786 (clone HIL-7R-M21)	BD Biosciences	Cat#563324; RRID:AB_2738138
Tim3-BB515 (clone 7D3)	BD Biosciences	Cat#565568; RRID:AB_2744368
CD16-BUV496 (clone 3G8)	BD Biosciences	Cat#612944; RRID:AB_2870224
CD27-BB660 (clone M-T271)	BD Biosciences, custom	Cat#624295
CD161-BB700 (clone DX12)	BD Biosciences	Cat#745791; RRID:AB_2743247
CD38-BB790 (clone HIT2)	BD Biosciences, custom	Cat#624296
CD39-BV605 (clone A1)	BioLegend	Cat#328236; RRID:AB_2750430
CD137-PECy5 (clone 4B4-1)	BD Biosciences	Cat#551137; RRID:AB_394067

CD19-PE-Cy5.5 (clone SJ25-C1)	Thermo Fisher	Cat#MHCD1918; RRID:AB_1465597
CD197 (CCR7)-BUV661 (clone 2-L1-A)	BD Biosciences	Cat#749824; RRID:AB_2874072
CD197 (CCR7)-PE-Cy7 (clone 3D12)	BD Biosciences	Cat#557648; RRID:AB_396765
CD4-APCH7 (clone RPA-T4)	BD Biosciences	Cat#560158; RRID:AB_1645478
CD40-BUV395 (clone 5C3)	BD Biosciences	Cat#565202; RRID:AB_2739110
CD56-BUV563 (clone NCAM16.2)	BD Biosciences	Cat#612928; RRID:AB_2870213
CD86-BUV737 (clone FUN-1)	BD Biosciences	Cat#612784; RRID:AB_2814790
CX3CR1-PE-Cy7 (clone 2A9-1)	BioLegend	Cat#341612; RRID:AB_10900816
CD28-BV480 (clone CD28.2)	BD Biosciences	Cat#566110; RRID:AB_2739512
CD141-BV605 (clone 1A4)	BD Biosciences	Cat#740421; RRID:AB_2740151
Sirpa-BV650 (clone SE5A5)	BD Biosciences	Cat#743565; RRID:AB_2741588
OX40-BV711 (clone Ber-ACT35)	BioLegend	Cat#350029; RRID:AB_2632863
CD11b-BV750 (clone ICRF44)	BD Biosciences, custom	Cat#747357; RRID:AB_2872054
CD123-BV786 (clone 7G3)	BD Biosciences	Cat#564196; RRID:AB_2738662
CD206-BB515 (clone 19.2)	BD Biosciences	Cat#564668; RRID:AB_2738882
CD32-BB700 (clone FLI8.26)	BD Biosciences	Cat#742216; RRID:AB_2871430
Lag3-PE (clone T47-530)	BD Biosciences	Cat#565617
CD163-PECF594 (clone GHI/61)	BD Biosciences	Cat#562670; RRID:AB_2737711
CD80-PECy5 (clone L307.4)	BD Biosciences	Cat#559370; RRID:AB_397239
CD1c-AF647 (clone F10/21A3)	BD Biosciences	Cat#565048; RRID:AB_2744318
CD11c-AF700 (clone B-ly6)	BD Biosciences	Cat#561352; RRID:AB_10612006
HLA-DR-APC-H7 (clone G46-6)	BD Biosciences	Cat#561358; RRID:AB_10611876
HLA-DR-APC-R700 (clone G46-6)	BD Biosciences	Cat#565127; RRID:AB_2732055
CXCR6-BUV563 (clone 13B 1E5)	BD Biosciences	Cat#748450; RRID:AB_2872866
CD45-BUV805 (HI30)	BD Biosciences	Cat#612891; RRID:AB_2870179
CCR8-BV711 (clone 433H)	BD Biosciences	Cat#747575; RRID:AB_2744146
CD195-BV786 (clone 3A9)	BD Biosciences	Cat#565001; RRID:AB_2739039
CD272-BB630-P (clone J168-540)	BD Biosciences, custom	Cat#624294
TIGIT-BB790 (clone 741182)	BD Biosciences, custom	Cat#624452
Streptatvidin-BB660-P2	BD Biosciences, custom	Cat#624295
IL-1R1-PE (polyclonal)	R & D Systems	Cat#FAB269P-100; RRID:AB_2124912
IL-18R1α-PECy7 (clone H44)	BioLegend	Cat#313812; RRID:AB_2800827
IL-1R2-APC (clone 34141)	R & D Systems	Cat#FAB663A; RRID:AB_10569839
CD273-BV421 (clone MIH18)	BD Biosciences	Cat#563842; RRID:AB_2738445
CD85k-BV480 (clone ZM3.8)	BD Biosciences	Cat#746718; RRID:AB_2743983
CD68-BV711 (cloneY1/82A)	BD Biosciences	Cat#565594; RRID:AB_2739297
CD274-BB660-P (clone MIH1)	BD Biosciences, custom	Cat#624295
Axl-PE (clone 108724)	R&D Systems	Cat#FAB154P
KI67-eFluor 660 (clone SolA15)	ThermoFisher Scientific	Cat#50-5698-80; RRID:AB_2574234
Granzyme B AF700 (clone QA16A02)	BioLegend	Cat#372222; RRID:AB_2728389
Human MR1 5-OP-RU BV421	NIH Tetramer Facility	
Human TruStain FcX (Fc-Block)	BioLegend	Cat#422302; RRID:AB_2818986
CD3-Ab-O (clone SK7)	BD Biosciences	Cat#940000; RRID:AB_2875891
CD4-Ab-O (clone SK3)	BD Biosciences	Cat#940001; RRID:AB_2875892
CD8-Ab-O (clone RPA-T8)	BD Biosciences	Cat#940003; RRID:AB_2875894
CD19-Ab-O (clone SJ25C1)	BD Biosciences	Cat#940004; RRID:AB_2875895
CD14-Ab-O (clone MϕP9)	BD Biosciences	Cat#940005; RRID:AB_2875896
CD16-Ab-O (clone 3G8)	BD Biosciences	Cat#940006; RRID:AB_2875897
CD56-Ab-O (clone NCAM16.2)	BD Biosciences	Cat#940007; RRID:AB_2875898
CD11b-Ab-O (clone M1/70)	BD Biosciences	Cat#940008; RRID:AB_2875899

CD25-Ab-O (clone 2A3)	BD Biosciences	Cat#940009; RRID:AB_2875900
HLA-DR-Ab-O (cloneG46-6)	BD Biosciences	Cat#940010; RRID:AB_2875901
CD45RA-Ab-O (clone HI100)	BD Biosciences	Cat#940011; RRID:AB_2875902
CD127-Ab-O (clone HIL-7R-M21)	BD Biosciences	Cat#940012; RRID:AB_2875903
CD38-Ab-O (clone HIT2)	BD Biosciences	Cat#940013; RRID:AB_2875904
CD279-Ab-O (clone EH12.1)	BD Biosciences	Cat#940015; RRID:AB_2875906
CD28-Ab-O (clone CD28.2)	BD Biosciences	Cat#940017; RRID:AB_2875908
CD27-Ab-O (clone M-T271)	BD Biosciences	Cat#940018; RRID:AB_2875909
CD69-Ab-O (clone FN 50)	BD Biosciences	Cat#940019; RRID:AB_2875910
CD123-Ab-O (clone 7G3)	BD Biosciences	Cat#940020; RRID:AB_2875911
CD45RO-Ab-O (clone UCHL1)	BD Biosciences	Cat#940022; RRID:AB_2875913
CD11c-Ab-O (clone B-Ly6)	BD Biosciences	Cat#940024; RRID:AB_2875915
CD86-Ab-O (clone FUN-1)	BD Biosciences	Cat#940025; RRID:AB_2875916
CD183-Ab-O (clone 1C6/CXCR3)	BD Biosciences	Cat#940030; RRID:AB_2875921
CD196-Ab-O (clone 11A9)	BD Biosciences	Cat#940033; RRID:AB_2875924
CD80-Ab-O (clone L307.4)	BD Biosciences	Cat#940036; RRID:AB_2875927
CD278-Ab-O (clone DX29)	BD Biosciences	Cat#940043; RRID:AB_2875934
CD194-Ab-O (clone 1G1)	BD Biosciences	Cat#940047; RRID:AB_2875938
CD40-Ab-O (clone 5C3)	BD Biosciences	Cat#940049; RRID:AB_2875940
CD137-Ab-O (clone 4B4-1)	BD Biosciences	Cat#940055; RRID:AB_2875946
TCRgd-Ab-O (clone B1)	BD Biosciences	Cat#940057; RRID:AB_2875948
CD163-Ab-O (clone GH1/61)	BD Biosciences	Cat#940058; RRID:AB_2875949
CD134-Ab-O (clone ACT35)	BD Biosciences	Cat#940060; RRID:AB_2875951
Tim3-Ab-O (clone 7D3)	BD Biosciences	Cat#940066; RRID:AB_2875957
CD103-Ab-O (clone Ber-ACT8)	BD Biosciences	Cat#940067; RRID:AB_2875958
CD206-Ab-O (clone 19.2)	BD Biosciences	Cat#940068; RRID:AB_2875959
CD32-Ab-O (clone FLI8.26)	BD Biosciences	Cat#940069; RRID:AB_2875960
CD161-Ab-O (clone DX12)	BD Biosciences	Cat#940070; RRID:AB_2875961
CD39-Ab-O (clone TU66)	BD Biosciences	Cat#970073; RRID:AB_2875964
CD141-Ab-O (clone 1A4)	BD Biosciences	Cat#940079; RRID:AB_2875970
Lag3-Ab-O (clone T47-530)	BD Biosciences	Cat#940080; RRID:AB_2875971
CD1c-Ab-O (clone F10/21A3)	BD Biosciences	Cat#940083; RRID:AB_2875974
CD244-Ab-O (clone 2-69)	BD Biosciences	Cat#940362; RRID:AB_2876232
CD274-Ab-O (clone B7-H1)	BD Biosciences	Cat#940035; RRID:AB_2875926
CX3CR1-Ab-O (clone 2A9-1)	BD Biosciences	Cat#940216; RRID:AB_2876098
VISTA-Ab-O (clone MIH65.rMAb)	BD Biosciences	Cat#940497; RRID:AB_2876339
CCR7-Ab-O (clone 2-L1-A)	BD Biosciences	Cat#940394; RRID:AB_2876258
CD5-Ab-O (clone UCHT2)	BD Biosciences	Cat#940038; RRID:AB_2875929
CD195-Ab-O (clone2D7/CCR5)	BD Biosciences	Cat#940050; RRID:AB_2875941
CXCR6-Ab-O (clone 13B 1E5)	BD Biosciences	Cat#940234; RRID:AB_2876115
CCR2-Ab-O (clone LS132.1D9)	BD Biosciences	Cat#940286; RRID:AB_2876163
Anti-PE-Ab-O (E31-1459)	BD Biosciences (custom)	Cat#2216Z / 120162

Supplementary Table 3

Custom gene panel for Rhapsody experiments (data shown in Figure 4)
For base panel, please refer to the "Human Immune Response Panel"
(BD Biosciences, #633750)

1	ADAM15		33	FCGR3B		65	MMP2
2	ADAM17		34	FOS		66	MNDA
3	ADAM28		35	FOXO3		67	MRC1
4	AHR		36	GATA3		68	MX1
5	AIF1		37	GZMM		69	MX2
6	ALCAM		38	HIF1A		70	MXRA8
7	AXL		39	HLA-DPB1		71	NLRP3
8	BATF		40	HLA-DQA1		72	PDCD1LG2
9	BIRC5		41	HOPX		73	PTPN6
10	C1ORF54		42	ICOSLG		74	S100A8
11	CAPG		43	ID2		75	S1PR1
12	CCL3L3		44	ID3		76	SBK1
13	CCL4L2		45	IFITM1		77	SERPINA1
14	CCR6		46	IFNGR2		78	SOCS3
15	CD200R		47	IFNL1		79	STK38
16	CD207		48	IL10		80	TGFBR2
17	CD40LG		49	IL10RB		81	TIMP1
18	CD68		50	IL18BP		82	TIMP2
19	CD83		51	IL23A		83	TIMP3
20	CDH1		52	IL27		84	TMEM123
21	CLEC9A		53	IL6R		85	TNFRSF14
22	CLU		54	IL6ST		86	TNFRSF18
23	CRTAM		55	IRF7		87	TNFRSF1B
24	CSF1		56	ITGA1		88	TNFSF12
25	CSF1R		57	ITGA5		89	TOX
26	CSF2RA		58	KLF2		90	TREM2
27	CTSK		59	KLF3		91	TSPAN18
28	CTSS		60	KLF6		92	VCAN
29	DUSP6		61	KLRC2		93	VEGFB
30	EBI3		62	KLRD1		94	XCL1
31	FBLN2		63	LYZ		95	XCL2
32	FBN2		64	MMP1		96	ZFP36